

1 Modeling tabular icebergs coupled to an ocean model

2 **A. A. Stern¹, A. Adcroft¹, O. Sergienko¹, G. Marques¹, R. Hallberg¹**

3 ¹Geophysical Fluid Dynamics Laboratory, Princeton University
4 ¹201 Forrestal Rd, Princeton, NJ 08540, USA

5 **Key Points:**

- 6
- 7
- 8
- 9
- 10
- A novel modeling framework is developed to explicitly model large tabular icebergs submerged in the ocean.
 - Tabular icebergs are constructed out of Lagrangian elements that drift in the ocean, and are held together by numerical bonds.
 - Breaking the numerical bonds allows us to model iceberg breakup and calving.

11 **Abstract**

12 Large tabular icebergs calved from Antarctic ice shelves have long lifetimes (due to their
 13 large size), during which they drift across large distances, altering regional ocean circulation,
 14 bottom-water formation, sea-ice formation and biological primary productivity in
 15 the icebergs' vicinity. However, despite their importance, the current generation of ocean
 16 circulation models is unable to represent large tabular icebergs. In this study we develop
 17 a novel framework to model large tabular icebergs submerged in the ocean. In this frame-
 18 work, tabular icebergs are composed of Lagrangian elements that drift in the ocean, and
 19 are held together and interact with each other via bonds. A break of these bonds allows
 20 the model to emulate calving events (i.e. detachment of a tabular iceberg from an ice
 21 shelf), and tabular icebergs breaking up into smaller pieces. Idealized simulations of a
 22 calving tabular iceberg, its drift, and of a tabular iceberg breaking into two pieces, demon-
 23 strate capabilities of the developed framework.

24 **1 Introduction**

25 Large tabular icebergs - pieces of floating ice with horizontal dimensions substan-
 26 tially larger than the vertical dimension - calve infrequently (~ every forty-fifty years)
 27 from Antarctic or Greenlandic ice shelves [Jacobs et al , 1992]. Observational estimates
 28 suggest that over the past 30 years approximately half of Antarctic ice-shelf decay is due
 29 to iceberg calving, while the other half occurs through ice-shelf melting [Depoorter et al
 30 , 2013; Rignot et al , 2013]. The infrequently-calved tabular icebergs (horizontal extent
 31 larger than 5 km) account for more than 90% of the Southern Hemisphere iceberg mass
 32 [Tournadre et al , 2016].

33 After calving, icebergs slowly drift away from their origins, often becoming stuck in
 34 sea ice, or grounding on bathymetric highs along the Antarctic coast [Lichéy and Hellmer
 35 , 2001; Dowdeswell and Bamber , 2007]. Large tabular icebergs extend deep into the wa-
 36 ter column, and have the potential to disrupt ocean circulation patterns for months or even
 37 years after calving [Robinson et al , 2012; Stern et al , 2015]. The freshwater flux from
 38 iceberg melt impacts ocean hydrography around the iceberg, influencing sea-ice produc-
 39 tion and bottom-water formation [Arrigo et al , 2002; Robinson et al , 2012; Nicholls et
 40 al , 2009; Fogwill et al , 2016]. Because of their large size, the tabular icebergs have long
 41 lifetimes during which they drift over long distances injecting meltwater along the way
 42 and impacting the Southern Ocean state (e.g. hydrography, sea ice conditions, etc.) far
 43 away from their calving origins [Stern et al , 2016]. Meltwater injection (and the accom-
 44 panying upwelling) from icebergs can also influence biological productivity by bringing
 45 nutrients to the surface ocean or changing sea ice conditions [Arrigo et al , 2002; Ver-
 46 net et al , 2012; Biddle et al , 2015]. The increased productivity associated with free-
 47 floating tabular icebergs has been linked with local increases in ocean carbon uptake, po-
 48 tentially large enough to be a significant fraction of the Southern Ocean carbon sequestra-
 49 tion [Smith et al , 2007].

50 In recent years, there has been an increased interest in iceberg drift and decay. This
 51 surge of interest has been driven by (i) the need to understand polar freshwater cycles
 52 in order to create realistic climate forecasts and sea level projections [Silva et al , 2006;
 53 Shepherd and Wingham , 2007; Rignot et al , 2013]; and (ii) the increased navigation and
 54 exploration activities in high-latitude iceberg-filled waters in the Arctic [Pizzolato et al ,
 55 2012; Unger , 2014; Henderson and Loe , 2016]. The increased interest in icebergs has
 56 led to the development of numerical models of iceberg drift and decay [Mountain , 1980;
 57 Bigg et al , 1997; Gladstone et al , 2001; Kubat et al , 2005], some of which have been
 58 included in global General Circulation Models [Martin and Adcroft , 2010; Marsh et al
 59 , 2015]. These iceberg drift models treat icebergs as Lagrangian point particles, which
 60 are advected by the flow, and melt according to certain parameterizations for icebergs
 61 melt. Since icebergs are treated as point particles, iceberg drift models are mostly suitable

for modeling icebergs smaller than an ocean grid cell. Consequently, these models have mostly been used to represent icebergs smaller than 3.5 km on a global scale [Jongma et al , 2009; Martin and Adcroft , 2010; Marsh et al , 2015].

Point-particle iceberg drift models are less suitable for modeling larger tabular icebergs, where the size and structure of the iceberg may be an important feature in determining their drift and decay [Stern et al , 2016]. They also are not suitable for studying the local effects that icebergs have on the surrounding ocean, or the small scale processes that influence iceberg melt and decay [Wagner et al , 2014; Stern et al , 2015]. For these reasons, tabular icebergs are currently not represented in the iceberg drift models used as components of climate models, despite accounting for the vast majority of the total Southern Hemisphere iceberg mass [Tournadre et al , 2016]. Point-particle iceberg models also do not have any representation of iceberg breakup and calving, which is known to be an important iceberg decay mechanism and influences iceberg trajectories.

The goal of this study is to develop a new framework to model all kinds of icebergs, where tabular icebergs are explicitly resolved in the ocean. Our new representation of icebergs aims to include the following key properties: (i) icebergs should be able to travel large distances within the ocean, (ii) icebergs should melt and decay as they drift in the ocean, (iii) icebergs should behave as if they have finite extent (so that we can use the model to study local effects that icebergs have on the surrounding ocean), and (iv) tabular icebergs should be able to break away from ice shelves or break into smaller pieces. Properties (i) and (ii) are common to point-particle iceberg models, while properties (iii) and (iv) are new to the framework developed in this study. A further requirement of the new framework is that the model should run sufficiently quickly to be used in general circulation models used for climate.

In order to allow icebergs to travel large distances, it is natural to model the icebergs in a Lagrangian framework (as in the point particle iceberg drift models described above). In our model we therefore represent icebergs using Lagrangian elements. However in our model icebergs are no longer treated as point particles that interact with the ocean at a single location, but rather icebergs are given physical structure, so that they interact with the ocean across multiple ocean grid cells, depress the ocean surface over a wide area, and can interact with other icebergs (see schematic in Figure 1). This is done by assigning a finite surface area and shape to the Lagrangian elements, which allows the elements to behave as if they have a finite extent. The finite extent of an element is transmitted by the ocean by distributing the element's weight, surface area and melt fluxes over multiple ocean grid cells in a way which is consistent with the shape of the ice element. The finite extent of an element is felt by other elements through repulsive forces which are applied when the boundaries of the elements overlap.

Large tabular icebergs can then be represented by ‘bonding’ together multiple ice elements using numerical bonds (see schematic in Figure 1). The numerical bonds hold the ice elements together and allow a collection of elements to move as a unit. This allows us to study how tabular icebergs drift in the ocean when forced by ocean currents and wind. An advantage of representing tabular icebergs using numerical bonds is that by manually breaking the bonds, we can simulate iceberg calving, allowing us to study the ocean response to tabular icebergs detaching from ice shelves (e.g.: Figure 2), or the response to an iceberg fracturing into multiple smaller pieces.

The manuscript is organized as follows. Section 2 gives a description of many of the key aspects of the model developed in this study. Since this model is a new approach to modeling icebergs, we present many of the technical aspects of the model. In Sections 3 and 4, we demonstrate the capabilities of the model by simulating a tabular iceberg detaching from an idealized ice shelf. In a further simulation we break some numerical bonds within the tabular iceberg to demonstrate an iceberg splitting in two.

113 **2 Model description**

114 The Lagrangian Bonded Iceberg Model (LBIM) is a Lagrangian particle-based model
 115 in that the objects of the model are Lagrangian elements. Each element represents a col-
 116 umn of ice that is floating in the ocean, and has a position, velocity, mass, and a set of
 117 dimensions, which can evolve in time. The motion of each element is determined by a
 118 momentum equation which is solved in the (Lagrangian) reference frame of the element.
 119 The elements experience oceanic and atmospheric forces, which are either prescribed, or
 120 computed by coupling the LBIM to an ocean/atmosphere model. The LBIM elements also
 121 interact with one another and can be bonded together to form larger structures. The an-
 122 gular momentum of the elements is not modeled explicitly; instead rotational motion of
 123 larger structures emerge as a consequence of bond orientation and collective motion.

124 In different contexts, the LBIM elements can be thought to represent individual ice-
 125 bergs, sea ice flows, or, when the elements are bonded together, they can represent larger
 126 structures such as tabular icebergs or ice shelves.

127 The LBIM is developed on the code base of an existing iceberg drift model [Martin
 128 and Adcroft , 2010; Stern et al , 2016]. When run with the correct set of runtime flags,
 129 the model runs as a traditional iceberg drift model.

130 **2.1 Equations of motion**

131 The elements drift in the ocean, in response to atmosphere, ocean and sea-ice drag
 132 forces, as well as the Coriolis force and a force due to the sea surface slope. When these
 133 ice elements move alone (without interactions with other elements), they can be thought
 134 of as representing individual (or clusters of) small icebergs, and follow the same equations
 135 described in the iceberg drift model of Martin and Adcroft [2010] (based on the equa-
 136 tions outlined in Bigg et al [1997] and Gladstone et al [2001]).

137 In addition to the external forces, the elements in the LBIM experience interactive
 138 forces due to the presence of other elements. Two types of interactive forces are included
 139 between elements. The first force is a repulsive force which is applied to elements to pre-
 140 vent them from overlapping the boundaries of the neighboring elements. The second in-
 141 teractive force is a force due to numerical ‘bonds’, and is only applied if two elements
 142 are labelled as ‘bonded’. When two elements are bonded, each element feels an attractive
 143 force that prevents the elements from moving too far apart from one another.

144 The momentum equation for each element is given by

$$M \frac{D\vec{u}}{Dt} = \vec{F}_A + \vec{F}_W + \vec{F}_R + \vec{F}_C + \vec{F}_{SS} + \vec{F}_{SI} + \vec{F}_{IA}, \quad (1)$$

145 where $\frac{D}{Dt}$ is the total (Lagrangian) derivative, M is the mass of the element, \vec{u} is the ve-
 146 locity of the element, and the terms on the right hand side give the forces on the element
 147 due to air drag (\vec{F}_A), water drag (\vec{F}_W), sea ice drag (\vec{F}_{SI}), Coriolis force (\vec{F}_C), wave ra-
 148 diation force (\vec{F}_R), sea surface slope (\vec{F}_{SS}), and interactions with other elements (\vec{F}_{IA}).
 149 The environmental forces are the same as those presented in Martin and Adcroft [2010],
 150 and are provided for completeness in Appendix A. The details of the interactive forces are
 151 provided in below.

152 **2.2 Interactive Forces**

153 The interactive forces in the LBIM model are used to (i) prevent the ice elements
 154 from overlapping and (ii) to connect multiple ice elements together so that the collection
 155 of elements moves as a rigid body. Modeling the collisions and movements of rigid ob-
 156 jects precisely, requires very small time steps and precise collision detection algorithms,
 157 which are very computationally expensive. Models using these methods are typically only

run for a few days or even a few seconds, and are used to study rapid processes like crack formation or ridging [Hopkins , 2004; Bassis and Jacobs , 2013; Rabatel et al , 2013)]. The tabular iceberg framework presented in this study is developed in order to be used in general circulation models used for climate, and therefore must be run for many years. In order to gain the required computational efficiency, we relax the requirement that icebergs must be perfectly rigid and that ice elements can not overlap. Instead, we model the interactive forces between ice elements using damped elastic forces, which can be calculated more rapidly.

The total interactive force on an element is calculated by adding together the interactions with all other elements, such that the interactive force on element i , $(\vec{F}_{IA})_i$ is given by:

$$(\vec{F}_{IA})_i = \sum_{j \neq i} (\vec{F}_{IA})_{ij}, \quad (2)$$

where $(\vec{F}_{IA})_{ij}$ is the force on element i by element j . Both bonded and repulsive interactions are modeled using elastic stresses with frictional damping. The elastic component of the force is a function of the distance between the two elements, while the frictional damping force depends on the relative velocity of the two elements.

To describe the forces between two elements, we begin by introducing some notation. Let \vec{x}_i , \vec{x}_j be the positions of elements i and j . The distance between elements i and j is

$$d_{ij} = |\vec{x}_i - \vec{x}_j|. \quad (3)$$

When calculating the interactive forces between elements, the elements are assumed to be circular. We define the interaction radius of an element by

$$R_i = \sqrt{\frac{A_i}{\pi}}, \quad (4)$$

where A_i is the planar surface area of element i . Using this, we define the critical-interactive-length scale,

$$L_{ij} = R_i + R_j, \quad (5)$$

which governs interactions between elements i and j . Repulsive forces are only applied when $d_{i,j} < L_{i,j}$, while for $d_{i,j} > L_{i,j}$ attractive bonded forces are applied when a bond exists between element i and j (see diagram in Figure 3). The interactive forces are designed such that (in the absence of other external forces) bonded particles will settle in an equilibrium position where elements are separated by $L_{i,j}$.

To aid in notation, we define a bond matrix B_{ij} such that $B_{ij} = 1$ if elements i and j are bonded together and $B_{ij} = 0$ otherwise. Using this notation, the interactive force $(\vec{F}_{IA})_{ij}$ on an element i by an element j is given by

$$(\vec{F}_{IA})_{ij} = \begin{cases} (\vec{F}_e)_{ij} + (\vec{F}_d)_{ij} & \text{if } d_{ij} \leq L_{ij} \\ (\vec{F}_e)_{ij} + (\vec{F}_d)_{ij} & \text{if } d_{ij} > L_{ij} \text{ and } B_{ij} = 1 \\ 0 & \text{if } d_{ij} > L_{ij} \text{ and } B_{ij} = 0 . \end{cases} \quad (6)$$

$(\vec{F}_e)_{ij}$ and $(\vec{F}_d)_{ij}$ are the elastic and frictional damping components of the interactive force between elements i and j . The elastic force $(\vec{F}_e)_{ij}$ between elements is given by

$$(\vec{F}_e)_{ij} = -\kappa_e (d_{i,j} - L_{i,j}) T_{i,j} \vec{r}_{ij}, \quad (7)$$

where $\vec{r}_{ij} = \frac{(\vec{x}_i - \vec{x}_j)}{|\vec{x}_i - \vec{x}_j|}$ is the directional unit vector between the position of element i and j , κ_e is the spring constant, and $T_{i,j}$ is the minimum of the thickness of elements i and j . The interactive forces obey Newton's 3rd Law (i.e.: $(\vec{F}_{IA})_{ij} = -(\vec{F}_{IA})_{ji}$). The minimum thickness, $T_{i,j}$, is preferred to the average thickness, since this means that for two bonded elements a fixed distance apart, the acceleration due to elastic forces is bounded, even when the thickness of one of the elements approaches zero.

196 The frictional damping force acts to oppose the relative velocity of the two particles.
 197 If \vec{r}_{ij}^\perp is the direction vector perpendicular to \vec{r}_{ij} , and $P_{\vec{r}_{ij}}$ and $P_{\vec{r}_{ij}^\perp}$ are the projection ma-
 198 trices that project onto \vec{r}_{ij} and \vec{r}_{ij}^\perp respectively, then the frictional damping force is given
 199 by

$$(F_d)_{ij} = \left(-c_{r\parallel} P_{\vec{r}_{ij}} - c_{r\perp} P_{\vec{r}_{ij}^\perp} \right) \cdot (\vec{u}_i - \vec{u}_j) \quad (8)$$

200 Here $c_{r\parallel}$ and $c_{r\perp}$ are the drag coefficients for the damping parallel and perpendicular to
 201 r_{ij} , respectively. We set $c_{r\parallel} = 2\sqrt{\kappa_e}$, so that the elastic force parallel to \vec{r}_{ij} is critically
 202 damped. The damping coefficient in the the perpendicular direction is set to $c_{r\perp} = \frac{1}{4}c_{r\parallel}$.
 203 The damping forces are implemented using an implicit time stepping scheme, to avoid
 204 stability issues for very small elements (details found in Appendix B).

205 Figure 4 illustrates the effectiveness of the repulsive forces in an uncoupled (ice-
 206 only) simulation of ice elements forced to drift westward into a bay. The elements eventu-
 207 ally come to rest in the bay with minimal overlap between elements. In this simulation we
 208 find that the frictional damping forces (both parallel and perpendicular to \vec{r}_{ij}) are needed
 209 to reduce the motion (vibrations) of particles packed tightly together at the coast. Fig-
 210 ure 5 illustrates the effectiveness of the numerical bonds in simulations of small icebergs
 211 (individual un-bonded elements) and large icebergs (constructed from many ice elements
 212 bonded together) forced to drift towards a convex coast line. When the tabular icebergs ar-
 213 rive at the coast, they bump into the coastline and begin to rotate, influencing the paths of
 214 the other icebergs (see movie S1 in the supplementary material). This example illustrates
 215 an advantage of using small elements bonded together, to represent large-scale structure
 216 and rotational motion without explicitly accounting for the angular momentum of the ele-
 217 ments (as discussed in Jakobsen [2001]).

218 2.3 Initializing element geometry and packing

219 For purposes of packing, we assume that elements have surface areas which are
 220 shaped as equally-sized regular hexagons (note that the elements are assumed to be cir-
 221 cular for proposes of interactions, but are assumed to be hexagonal for packing purposes).
 222 When packing these elements together, the hexagonal elements are initially arranged in
 223 a staggered lattice, with each element bonded to the adjacent elements (Figure 6a). In
 224 this arrangement, each element (away from the edges) is bonded to six other elements.
 225 The bonds between elements form a pattern of equilateral triangles, which give the larger
 226 structure rigidity. The circular shape of elements (used for interactions) is inscribed within
 227 the hexagonal shape used for packing (Figure 6a). The centers of adjacent elements are
 228 initially separated by a distance $d_{i,j} = L_{i,j} = 2A_p$, where A_p is the length the apothems
 229 of the hexagons.

230 Some experiments were also performed using rectangular elements, arranged in a
 231 regular (non-staggered) lattice. In this case, each element forms four bonds with adjacent
 232 elements. However, the resultant structures were found to be much less rigid and tended
 233 to collapse when sufficient forces was applied. For this reason, hexagonal elements are
 234 used here.

235 2.4 Ocean-ice and ice-ocean coupling

236 The LBIM is coupled to the ocean model via a two-way synchronous coupling,
 237 meaning that ocean-model fields are passed to the LBIM, and the LBIM fields are passed
 238 back to the ocean model at every time step. Passing fields between the two models in-
 239 volves interpolating the fields from the ocean model's Eulerian grid onto the LBIM's 'La-
 240 grangian grid' (i.e.: onto the ice elements), and aggregating fields from the Lagrangian
 241 elements onto the ocean-model's Eulerian grid.

242 The coupling from the ocean model to the LBIM is straight forward: at every time
 243 step: the ocean mixed layer temperature, salinity, velocity and sea-ice concentration are
 244 passed from the ocean model to the LBIM, to be used in the momentum and thermo-
 245 dynamic equations of the ice elements. Since tabular icebergs are explicitly resolved in
 246 the ocean, it is sufficient for each element to interact with ocean mixed layer only (i.e.:
 247 there is no need to manually embed icebergs into the ocean by integrating ocean fields
 248 over the icebergs' thickness, as suggested in Merino et al [2016]). Within the LBIM, the
 249 ocean model fields are interpolated onto the Lagrangian grid using a bilinear interpolation
 250 scheme.

251 The LBIM influences the ocean by: (i) applying a pressure to the ocean surface, (ii)
 252 affecting the upper ocean by applying a no-slip boundary condition and frictional velocity
 253 beneath the ice, and (iii) imposing heat, salt and mass fluxes on the ocean, associated with
 254 ice melting. Six fields are passed from the LBIM to the ocean model: ice mass, ice area,
 255 frictional velocity, and heat, salt and mass fluxes. Fields from the LBIM are aggregated
 256 from the Lagrangian elements to the Eulerian ocean grid before they are passed to the
 257 ocean model.

258 The aggregation of the LBIM fields onto the ocean grid is done in a way that is
 259 consistent with the shape of the elements in the LBIM (see Section 2.3). Fields are ‘spread’
 260 to the ocean model grid by exactly calculating what fraction of an element’s surface area
 261 lies in a particular grid box, and dividing the field in proportion to this fraction. As an
 262 example, consider a hexagonal element in the LBIM, which is positioned such that it in-
 263 tersects four ocean grid cells (Figure 6b). In this situation, the element’s mass (for exam-
 264 ple) is divided between these four ocean cells in proportion to the overlap area between
 265 the hexagonal element and the grid cell (this fraction is shown by the colors in Figure
 266 6b). An advantage of this approach is that there are no jumps in pressure as an element
 267 moves from one grid cell to another, which could trigger artificial tsunamis within the
 268 ocean model, making the ocean model unrealistic.

269 The numerical calculation of the intersection between hexagons and the ocean grid
 270 is simplified by dividing the hexagon into 6 equilateral triangles. This method allows for
 271 the intersection to be found even when the hexagon is not aligned with the grid.

272 The aggregation scheme is coded with the restriction that an element’s area can only
 273 intersect a maximum of four ocean grid cells at a time. A consequence of this is that this
 274 sets a limit on the maximum size of elements that can be represented using this model,
 275 i.e.: the longest horizontal dimension of an ice element must be smaller than the ocean
 276 grid spacing. Larger ice structures are constructed by bonding together smaller elements.

277 2.5 Melting parameterization

278 The ice elements change their mass and size due to melting, which also affects the
 279 surrounding ocean by changing its heat and salt content. In the model, these processes are
 280 parametrized in several ways. In this section we described the melt parametrization for
 281 bonded, unbonded and partially bonded elements.

282 As mentioned above, ice elements which do not interact with other elements are
 283 modeled identically to the point particle icebergs described in Martin and Adcroft [2010].
 284 These elements melt according to three semi-empirical parametrization for melt commonly
 285 used in previous iceberg studies [Gladstone et al , 2001; Martin and Adcroft , 2010].
 286 Three types of iceberg melting are distinguished: basal melt, M_b , melt due to wave ero-
 287 sion, M_e and melt due to buoyant convection, M_v . M_e and M_v are applied to the sides of
 288 the ice element, while M_b is applied at the ice element base. The details of M_b . M_v and
 289 M_e are given in Appendix A.

When multiple elements are bonded together to form larger structures, it is no longer appropriate to use the parameterizations for melt developed for individual point-particle icebergs. An element which is completely surrounded by other elements, is meant to represent a column of ice in the middle of a large structure, and hence will not experience melt at its sides due to wave erosion or buoyant convection. Also, the iceberg basal melt rate, M_b described above is based on boundary layer theory of flow past a finite plate, and is only appropriate for basal surfaces where the distance from the leading edge is sufficiently small [Eckert , 1950; Weeks and Campbell , 1973]. For an element in the interior of a large structure, the distance from the edge of the structure is large, and so using M_b for the basal melt is not appropriate. Instead, the basal melt, M_s is determined using the three equation model for basal melt, which is a typical melting parametrization used beneath ice shelves [Holland and Jenkins , 1999].

When using both individual elements and bonded elements in the same simulation, we determine which melt rate parameterizations to use based on the amount of bonds that each element has. An element in the center of a large structure has the maximum number of bonds, while un-bonded elements has no bonds. If an element can have maximum number of bonds N_{max} , and the number bonds that an element has is N_b , then this element experiences the side melt and bottom melt

$$M_{side} = \frac{(N_{max} - N_b)}{N_{max}}(M_v + M_e) \quad (9)$$

and

$$M_{bottom} = \frac{(N_{max} - N_b)}{N_{max}}M_b + \frac{N_b}{N_{max}}M_s \quad (10)$$

respectively. In this way, elements with no bonds, melt like point-particle icebergs; elements at the center of large structures melt like ice shelves; and elements at the sides of large structures have a combination of iceberg side and basal melt, and ice-shelf melt.

2.6 Algorithms and computational efficiency

Including interactions between elements leads to an increase in the computational complexity of the model. In this subsection we comment on some of the algorithmic procedures that have been used to increase the computational efficiency.

2.6.1 Interactions and Bonds

At every time step, we calculate the force on each element due to interactions with every other element. This involves order N^2 operations (for N elements). However, since each element only has repulsive interactions with elements that are less than one ocean grid cell away, and each element only has bonded interactions with a small number of other elements, we are able to reduce the number of computations.

This is achieved by storing the element data in an efficient way that eliminates a search through all element pairs to check if they are close to one another or are bonded with one another. The data storage system is organized as follows: pointers to the memory structures containing each element are stored in linked list data structures, which allow elements to be added and removed from the lists easily without restructuring the entire list. Instead of using one list for all the elements on a processor (as was done in the original code [Martin and Adcroft , 2010]), we use a separate linked list for each ocean grid cell. When an element moves between ocean grid cells, it is removed from its original list and added to the list corresponding to its new ocean grid cell. Since the area of elements has to be smaller than the area of an ocean grid cell, the critical interaction length scale (equation 5) is less than the size of a grid cell. This means that elements only experience repulsive forces with other elements in the same ocean grid cell, or in one of the 8 adjacent cells. At each time step and for each element i , the code traverses the linked lists of

335 the 9 surrounding grid cells, and applies a repulsive force if $d_{i,j} < L_{ij}$ (whether the ele-
 336 ments are bonded or not). Limiting the possible repulsive interactions to elements in these
 337 9 linked lists substantially reduces the computational time needed to calculate the total
 338 interactive forces.

339 The attractive forces are computed in a following way. Each bond is assigned a
 340 piece of memory. Each ice element contains a linked list of each of its bonds (typically
 341 up to six bonds per element). At every time step, the code traverses the lists of bonded
 342 elements, and adds an attractive bonded force corresponding to these bonds if $d_{i,j} > L_{ij}$
 343 (the repulsive bonded force to be applied when $d_{i,j} < L_{ij}$ is already accounted for by
 344 the procedure outlined in the previous paragraph). Having a list of bonds stored with each
 345 element reduces the computations needed for bonded interactions from order N^2 to or-
 346 der N. Computing attractive forces separately from the repulsive forces allows us to avoid
 347 checking whether two elements are bonded, which further increases the computational effi-
 348 ciency.

349 **2.6.2 Parallelization and halos**

350 The LBIM runs on multiple processors in parallel (using the same grid decomposi-
 351 tion as the ocean model). When elements move from an ocean cell on one processor to
 352 an ocean cell on a second processor, the memory has to be passed from one processor the
 353 next, added and removed to the appropriate lists and the memory has to be allocated and
 354 deallocated correctly. Element interactions across the edge of processors are handled using
 355 computational halos. A computational halo is a copy of the edge of a one processor which
 356 is appended to the edge of a second processor, so that the first processor can interact with
 357 the second processor during a time step. Before each time step, elements at the edges of
 358 each processor are copied onto the halos of adjacent processors so that they can be used
 359 in calculating the interactive forces. After each time step, these halos are removed, and
 360 the process is repeated. These halo updates are one of the most computationally expensive
 361 parts of the LBIM. Details of how the bonds are broken and reconnected across processor
 362 boundaries are provided in Appendix C.

363 **2.6.3 Time stepping**

364 The elements in the LBIM are advected using a semi-implicit velocity Verlet time-
 365 stepping scheme. The velocity Verlet time stepping scheme is commonly used in discrete
 366 element models in video games because it is computational efficient and has desirable
 367 stability properties [Jakobsen , 2001]. This time stepping scheme was preferred to the
 368 Runge-Kutta 4, which was used in the iceberg model of Martin and Adcroft [2010] since
 369 the Verlet time stepping only requires one calculation of the interactive forces once per
 370 time step (while the Runge-Kutta scheme requires the interactive forces to be calculated
 371 four times). Since the calculation of the interactive forces is one of the most computa-
 372 tionally expensive part of the algorithm, the Verlet scheme leads to a significant increase in
 373 the computational efficiency of the model. The Verlet scheme used in the LBIM contains
 374 a modification of the original (fully explicit) velocity Verlet time stepping scheme in that
 375 damping terms are treated implicitly (which increases the numerical stability). The details
 376 of this time stepping schemed are outline in Appendix B.

377 **3 Experiment Setup**

378 The introduction of Lagrangian elements, numerical bonds and interpolation schemes
 379 between the Eularian and Lagrangian grids (discussed in Section 2) means that we now
 380 have the tools to model large tabular icebergs submerged in the ocean. We demonstrate
 381 this capability by simulating a tabular iceberg drifting away from an ice shelf in idealized
 382 setting.

383 **3.1 Model configuration**

384 We use the geometric setup of the Marine Ice Ocean Modeling Inter-comparison
 385 Project (MISOMIP) [Asay-Davis et al , 2016]. The configuration consists of an idealized
 386 ice shelf in a rectangular domain. The domain is $L_x = 80$ km wide and $L_y = 480$ km
 387 long, and contains an ice shelf which is grounded on the south side of the domain and
 388 has an ice front at $y=650$ km. The ice thickness and bottom topography of this setup are
 389 shown in Figure 7a and 7c respectively, with the grounding line position drawn in for ref-
 390 erence. The configuration is the same as that of the Ocean0 setup in the MISOMIP, with a
 391 few minor changes to the ice-shelf geometry (see Supplementary Material for details).

392 **3.2 Initializing Lagrangian elements:**

393 The idealized ice shelf is constructed out of Lagrangian ice elements. Ice elements
 394 are hexagonal and are arranged in a regular staggered lattice (as discussed in Section 2.3).
 395 The sides of the hexagons are initialized with length $S = 0.98$ km. Gaps along the bound-
 396 aries are filled in using smaller elements so that the total ice-shelf area is preserved. The
 397 initial mass of the ice elements is determined by a preprocessing inversion performed be-
 398 fore the model is run. When the model runs, the mass of elements is aggregated from the
 399 Lagrangian grid onto the Eulerian ocean grid (see Section 2.3), and is used to find the
 400 surface pressure and ice draft (part of an ice column submerged into the ocean). The ice
 401 draft calculated without the aggregation (treating elements as point masses) contains large
 402 grid artifacts (Figures 7b). These grid artifacts are much reduced after the mass-spreading
 403 aggregation is used (Figure 7c).

404 **3.3 Ocean model setup**

405 The LBIM is coupled to the MOM6 ocean model [Hallberg et al , 2013]. The ocean
 406 model configuration uses a vertical coordinate system which is a hybrid between a sigma-
 407 level and a z-level coordinate. In particular, model layers deform underneath the ice shelf
 408 as they would in a sigma-coordinate model, but collapse to zero thickness when they in-
 409 tersect with bottom topography, as they would in a z-level model. The coordinate system
 410 was achieved using ALE regridding-remapping scheme [White et al , 2009]. The model
 411 uses a horizontal resolution of 2 km, and 72 vertical layers. All simulations were repeated
 412 using the ocean model configured in isopycnal mode (results were similar and are not pre-
 413 sented here).

414 Ocean parameters are as specified in the MISOMIP configuration [Asay-Davis et
 415 al , 2016], and are shown in Table 1. The simulation is initially at rest, with horizontally
 416 uniform initial ocean temperature and salinity profiles which vary linearly between spec-
 417 ified surface and bottom values: $T_{top} = -1.9^\circ$ C, $T_{bottom} = 1.0^\circ$ C, $S_{top} = 33.8$ psu,
 418 $S_{bottom} = 34.7$ psu. The maximum ocean depth is $H_{ocean} = 720$ m. A sponge layer is
 419 used on the northern boundary of the domain, which relaxes the temperature and salinity
 420 back to the initial temperature and salinity profile. The sponge layer has length L_{sponge}
 421 = 10 km, and has a relaxation time scale parameter $T_{sponge} = 0.1$ days at the northern
 422 boundary. The inverse of the relaxation time scale parameter drops linearly to zero over
 423 the length of the sponge layer. Melting is set to zero for ocean cells where the ocean col-
 424 umn thickness is less than 10m to avoid using more energy to melt ice than is present in
 425 the water column.

426 **3.4 Spinup period:**

427 The model is spun-up for 5 years with all ice elements being fixed. During spinup,
 428 the injection of buoyant meltwater at the base of the ice shelf drives a clockwise circu-
 429 lation within the domain (not shown). The circulation compares well with an identical
 430 static ice-shelf experiment run using an Eulerian ice shelf model [Goldberg et al , 2012].

431 A detailed comparison of the Lagrangian and Eulerian ice shelf models is presented in a
 432 separate study, and is not shown here.

433 3.5 Iceberg calving:

434 After spinup, a large tabular iceberg detaches from the ice shelf, and is allowed to
 435 drift into the open ocean. This is achieved by allowing all ice elements initially within a
 436 14.4 km radius of the center of the ice front to move freely while the other ice elements
 437 continue to be held stationary. Ice elements less than 12 km from the center of the ice
 438 front, are bonded together to form a semi-circular tabular iceberg. A ring of elements
 439 whose distance, d , from the ice front center obeys $12 \text{ km} \leq d \leq 14.4 \text{ km}$, are allowed
 440 to move freely, but have all their bonds removed. Elements in this half annulus represent
 441 fragments of the ice shelf which calve into small pieces during the calving event.

442 After the spinup period, a wind stress $\vec{\tau} = \langle \tau_x, \tau_y \rangle = \langle 0.05, 0.05 \rangle \frac{\text{N}}{\text{m}^2}$ is applied to
 443 drive the tabular iceberg away from the ice-shelf cavity. This is referred to as the control
 444 simulation. Perturbation experiments were also performed using other wind stress values.
 445 Further perturbation experiments were performed by breaking some numerical bonds in
 446 order to break the tabular iceberg into smaller pieces.

447 4 Model Results

448 After spinup, the elements near the ice-shelf front are allowed to move freely, and
 449 the icebergs begin to drift away from the ice shelf while fully submerged in the ocean
 450 (see Figures 2 and 8, and the animations in the supplementary materials). At this point,
 451 the LBIM and the ocean model are fully coupled: changes to the iceberg position alter
 452 the top-of-ocean pressure and dynamical boundary condition; and changes to the iceberg
 453 melt rates alter the top-of-ocean temperature, salt and mass fluxes. These changing ocean
 454 boundary conditions influence the ocean by triggering gravity waves, driving surface mix-
 455 ing, and affecting the ocean stratification. The evolving ocean velocities, temperatures
 456 and salinities feedback onto the ice elements by changing the force balance on the ice
 457 elements (leading to changes in the elements' position), and altering the melt rates. The
 458 various feedbacks within this coupled system offer many opportunities for the model to
 459 become unstable. The fact that the model is stable and that we are able to simulate tabu-
 460 lar icebergs moving in the ocean without the modeling crashing and introducing artificial
 461 effects like tsunamis, is a non-trivial technical milestone.

462 4.1 Iceberg motion

463 In the control simulation, the semi-circular tabular iceberg moves as a cohesive unit
 464 due to the presence of the numerical bonds, while the smaller ice fragments quickly dis-
 465 perse (Figure 2). The tabular iceberg drifts towards the north east, driven by the wind and
 466 steered by the Coriolis force. As the tabular iceberg drifts northwards, it rotates in a coun-
 467 terclockwise direction (the direction of the Coriolis force in the Southern Hemisphere),
 468 and makes contact with the eastern boundary of the domain, before continuing northward.
 469 Most of the smaller ice fragments also move to the northeast, but not as a cohesive unit.
 470 Some of these element also move to other parts of the domain.

471 The direction (and speed) of the iceberg drift is largely determined by the wind
 472 speed and direction. Perturbation experiments using different wind stresses show that for
 473 sufficiently large winds, the tabular iceberg drifts to the north east when $\tau_x > 0$, and to the
 474 north west when $\tau_x < 0$ (not shown). For a purely zonal wind stress with $|\tau_x| \leq 0.01 \frac{\text{N}}{\text{m}^2}$,
 475 the iceberg does not move away from the ice shelf. When the wind is purely offshore
 476 ($\tau_x = 0.0 \frac{\text{N}}{\text{m}^2}$), a meridional wind stress $\tau_y \geq 0.05 \frac{\text{N}}{\text{m}^2}$ is needed to move the tabular ice-
 477 berg away from the ice shelf. While this result is partly an artifact of the chosen shape
 478 of the calving iceberg, it is also consistent with Bassis and Jacobs [2013] who noted that

479 calving is a two step process consisting of (i) ice-shelf rifting that forms an iceberg and
 480 (ii) iceberg detachment. The results here suggest that strong (cross-shore) winds may be
 481 required to drive large tabular icebergs away from their source ice shelves.

482 **4.2 Breaking bonds**

483 The numerical bonds in the LBIM enable the tabular iceberg to retain its shape.
 484 This is demonstrated by comparing the control simulation to an identical simulation where
 485 all numerical bonds have been removed (Figure 9). In the bond-free simulation, the ice
 486 elements disperse and the calved iceberg quickly loses its original structure. This bond-free
 487 simulation does not adequately represent tabular iceberg, which can move long distances
 488 through the ocean as a cohesive unit. This result motivates the inclusion of numerical in
 489 the LBIM model, even though they are computationally expensive.

490 By breaking some (but not all) numerical bonds, we can simulate breaking of tab-
 491 ular icebergs into smaller pieces. Figure 10 shows the results of an experiment which is
 492 identical to the control experiment, except that all numerical bonds that intersect the line
 493 $x = \frac{L_x}{2}$ have been severed. This effectively cuts the large tabular iceberg into two halves.
 494 As the icebergs drift northwards, the two halves of the tabular iceberg each move as a co-
 495 hesive unit, but they are able to move independently of one other (Figure 10). The two
 496 large fragments initially move together, but begin to separate after a few days. The break-
 497 ing of a tabular iceberg has the additional effect of increasing the total surface area of ice
 498 exposed to the ocean, thus increasing the total decay rate of the icebergs.

499 **4.3 Ocean response**

500 Since the tabular iceberg is submerged in the ocean, the iceberg calving and drift
 501 affects the surrounding ocean. In the control simulation, as the tabular iceberg drifts north-
 502 ward a warming of the surface waters is observed around the tabular iceberg, with the
 503 largest warming occurring at the ice-shelf front and along the tabular iceberg's rounded
 504 edge (Figure 2). This surface warming is caused by upwelling of the warmer waters from
 505 beneath the ice shelf and iceberg. As the icebergs drifts away from the ice shelf, these
 506 warmer waters remain at the surface, mapping out the iceberg wake (Figure 2). The mo-
 507 tion of the tabular iceberg disturbs the ocean surface, which affects ocean velocities through
 508 out the water column (Figure 11). The elevated shears around the tabular iceberg lead to
 509 increased vertical mixing in the vicinity of the iceberg, which alters the stratification of
 510 the water column (Figure 8), warming the upper ocean. The signature of upwelling wa-
 511 ter in the wake of a drifting tabular iceberg bears some similarity to satellite observations
 512 of streaks of increased ocean color in the wake of tabular iceberg in the Southern Ocean
 513 [Duprat et al , 2016], suggesting that the increased productivity around icebergs may be
 514 driven by upwelling water delivering nutrients to the surface.

515 **4.4 Iceberg melt rates**

516 The increased subsurface velocities and temperatures cause elevated melt rates at
 517 the base of the ice shelf and iceberg (Figure 12). The largest melt rates are observed at
 518 the newly calved ice-shelf front and on the rounded side of the tabular iceberg (Figure
 519 12a), where the iceberg calving has created steep ice cliffs. These sharp ice fronts allow
 520 for large ocean currents (Figure 12c), which drive the elevated melt rates. The elevated
 521 melt rates act to smooth out the ice front over time, making the ice cliff less steep. While
 522 this is likely a real phenomena that could be observed in nature, we should be wary of
 523 the modeled velocities at the ice cliffs, since large changes in ice thicknesses are often
 524 associated with numerical pressure gradient errors which can drive spurious motion.

525 The large melt rates along the ice edges are also partly driven by the fact that dif-
 526 ferent melt parametrization are used in the interior and edges of large ice structures (see

527 Section 2.5). Figure 13 shows the melt rates computed with (a) the 3-equation-model
 528 parametrization [Holland and Jenkins , 1999], (b) point-particle-iceberg-melt parametriza-
 529 tion [Gladstone et al , 2001], and (c) the mixed-melt-rate parametrization (introduced in
 530 Section 2.5). The 3-equation-model melt rates (Figure 13a) are less than a third of the
 531 size of those calculated using the point-particle-iceberg-melt parametrization (Figure 13b).
 532 When the mixed-melt-rate parametrization is used (Figure 13c), the very high melt rates
 533 are only observed at the edges of ice structures.

534 5 Summary

535 In this study we present a novel framework for simulating tabular icebergs in ocean
 536 models. In this framework, large tabular icebergs are represented by collections of La-
 537 grangian elements that are held together by numerical bonds. Such a representation al-
 538 lows the icebergs to interact with the ocean across a wide area (larger than a grid cell),
 539 and behave as if they had a finite extent and structure. This is in contrast to previous rep-
 540 resentations of icebergs in numerical models [Jongma et al , 2009; Martin and Adcroft ,
 541 2010; Marsh et al , 2015] that treat icebergs as point particles. Explicitly resolving tabu-
 542 lar icebergs in the ocean allows the icebergs to interact with the ocean in a more realistic
 543 way, and allows us to study the effects that tabular icebergs have on ocean circulation. In-
 544 cluding numerical bonds between elements allows for simulations which emulate iceberg
 545 calving and fracture by severing the bonds.

546 The capabilities of the tabular iceberg model are demonstrated by modeling a tabular
 547 iceberg drifting away from an idealized ice shelf (also constructed using Lagrangian el-
 548 ements). The results show that explicitly resolving tabular icebergs in the ocean allows
 549 for a complex interaction between the iceberg and the surrounding ocean. In our con-
 550 trol setup, a tabular iceberg is driven away from the ice shelf by ocean currents, wind
 551 stress, and the Coriolis force. As the iceberg moves through the water, it disturbs the
 552 ocean surface, driving ocean currents. The motion of the iceberg and melt beneath the
 553 iceberg drive upwelling along the sides of the iceberg, which entrains ambient water and
 554 causes a warming of the surface ocean in the wake of the iceberg. The changing ocean
 555 conditions feed back onto the iceberg, affecting its motion and melt rates. The highest
 556 melt rates are observed at edge of the iceberg which has the steepest ice cliff. These have
 557 the effect of smoothing out the ice edge over time. Simulations without using numerical
 558 bonds showed that the bonds are essential for allowing the iceberg to move as a unit. We
 559 also demonstrate that by breaking these numerical bonds we can simulate iceberg fracture,
 560 which is important process that increases the rate of iceberg decay.

561 To our knowledge, the model presented in this study is the first model to explicitly
 562 resolve drifting tabular icebergs in an ocean model that can be used for climate studies. A
 563 natural extension of this work is a representation of tabular icebergs in a general circula-
 564 tion model (GCM). However, before this can be done, there are a number of issues that
 565 need to be resolved: firstly, the question of how and when to introduce tabular icebergs
 566 into the ocean needs to be addressed. For GCM's with active ice shelves, a calving law is
 567 needed to release the tabular iceberg into the ocean. The question of what calving law to
 568 use is a topic of ongoing research [Benn et all , 2007; Alley et al , 2008; Levermann et al
 569 , 2012; Bassis and Jacobs , 2013] and is still unresolved. One potential way to temporarily
 570 bypass this problem would be to run hindcast simulations using historically observed calv-
 571 ing events. A related issue is the question of how and when to break the bonds within the
 572 freely floating icebergs to simulation iceberg breakup. Without a rule for iceberg breakup,
 573 the tabular icebergs would likely drift to unrealistically low latitudes. Another challenge
 574 will be to develop methods to initialize the size and positions of elements on a spherical
 575 grid. This study used a cartesian coordinate system, which allowed us to initialize the ice
 576 elements in a regular staggered lattice. A different initialization method will be needed to
 577 generalize this initialization procedure to curved coordinates which are needed for large-
 578 scale global simulations. Further work is also needed to understand (and model) the in-

teractions between tabular icebergs and sea ice, and to parametrize the effects of iceberg grounding, as these interactions play a large role in dictating the trajectories of tabular icebergs. However, despite these remaining challenges, the technical framework described in this article is potentially a useful step towards including tabular icebergs in global GCM's, and hence a step towards making more accurate projections of future sea level.

6 Appendix A

6.1 Environmental forces on ice elements

The non-interactive forces on an ice element are as described in [Martin and Adcroft , 2010], and are repeated here for completeness. The forces on an element due to air (a), ocean (o) and sea ice (si) drag are given by

$$(\vec{F}_a) = \rho_a (0.5c_{a,v}WF + c_{a,h}LW)|\vec{u}_a - \vec{u}|(\vec{u}_a - \vec{u}), \quad (11)$$

$$(\vec{F}_o) = \rho_o (0.5c_{o,v}W(D - T_{si})F + c_{o,h}LW)|\vec{u}_o - \vec{u}|(\vec{u}_o - \vec{u}), \quad (12)$$

$$(\vec{F}_{si}) = \rho_{si} (0.5c_{si,v}WT_{si}F + c_{si,h}LW)|\vec{u}_{si} - \vec{u}|(\vec{u}_{si} - \vec{u}). \quad (13)$$

Here ρ_a , ρ_o , ρ_{si} , are the density of air, ocean and sea ice, respectively. $c_{a,v}$, $c_{o,v}$ and $c_{si,v}$ are the vertical drag coefficients with air, ocean and sea ice, while $c_{a,h}$, $c_{o,h}$ and $c_{si,h}$ are the respective horizontal drag coefficients. \vec{u}_a , \vec{u}_o , \vec{u}_{si} , are the velocities air, ocean and sea ice, respectively. L, W, T, F and D are the length, width, thickness, free-board and draft of the ice element. The element thickness is related to the draft and free-board by $T = F + D$ and $D = \frac{\rho}{\rho_o}T$, where ρ is the ice element density. T_{si} is the sea ice thickness.

The wave radiation force (\vec{F}_R) is given by

$$\vec{F}_R = \frac{1}{2}\rho_o c_{wd} g a \min(a, F) 2 \frac{WL}{W+L} \frac{\vec{v}_a}{|\vec{v}_a|} \quad (14)$$

where g is the acceleration due to gravity, a is the wave amplitude empirically related to the wind speed by $a = 0.010125|\vec{v}_a - \vec{v}_o|$, and c_{wd} is the wave drag coefficient defined as

$$c_{wd} = 0.06 \min\left(\max\left[0, \frac{L - L_c}{L_t - L_c} \right], 1 \right), \quad (15)$$

where $L_w = 0.32|\vec{v}_a - \vec{v}_o|^2$ is an empirical wave length, $L_c = 0.125L_w$ is the cutoff length, and $L_t = 0.25L_w$ is the upper limit.

The pressure gradient force is approximated as a force due to sea surface slope and given by

$$\vec{F}_{SS} = -Mg\vec{\nabla}\eta \quad (16)$$

where η is the sea surface height.

6.2 Melt rate parametrization

As discussed in Section 2.5, unbounded ice elements in the LBIM decay according to parameterizations for iceberg decay typically used in iceberg drift models [Martin and Adcroft , 2010], while ice elements within larger ice structures have only a basal melt given by the three equation model [Holland and Jenkins , 1999] .

For unbonded ice elements, the element thickness decays due to basal melt at a rate M_b , while the length and width of the elements decay as a result of melt due to wave erosion, M_e , and melt due to buoyant convection, M_v . Following Gladstone et al [2001] and

Martin and Adcroft [2010], the basal melt rate, wave erosion melt rate, and buoyant convection melt rate are parameterized by

$$M_b = 0.58|\vec{v} - \vec{v}_0|^{0.8} \frac{\tilde{T}_0 - \tilde{T}}{L^{0.2}} \quad (17)$$

$$M_e = \frac{1}{12} S_s \left(1 + \cos [\pi A_i^3] \right) \left(\tilde{T}_0 + 2 \right), \quad (18)$$

$$M_v = \left(7.62 \times 10^{-3} \right) \tilde{T}_0 + \left(1.29 \times 10^{-3} \right) \tilde{T}_0^2. \quad (19)$$

\tilde{T} is the effective iceberg temperature and is set to $\tilde{T} = 4^\circ\text{C}$, \tilde{T}_0 is the temperature at the top of the ocean, A_i is the sea-ice area fraction, and S_s is the sea state, which is given by the Beaufort scale

$$S_s = \frac{2}{3} |\vec{u}_a - \vec{u}_o|^{\frac{1}{2}} + \frac{1}{10} |\vec{u}_a - \vec{u}_o| \quad (20)$$

All three melt rates are in units of meters per day.

For elements inside larger structures, the melt due to wave erosion and melt due to buoyant convection are set to zero, and the basal melt, M_s , is given by the standard three equation model [Holland and Jenkins , 1999].

7 Appendix B

7.1 Modified Verlet Algorithm

The LBIM uses a version velocity Verlet time-stepping algorithm, which has been modified to allow part of the forcing to be calculated implicitly. The traditional velocity Verlet algorithm is commonly used in molecular dynamics, as it is simple to implement, second order accurate and computationally efficient [Swope et al , 1982; Omelyan et al , 2002]. Here we modify the traditional scheme to allow for the drag forces to be modeled implicitly, which prevents large accelerations for element's whose mass approaches zero. To do this, we include both an implicit and explicit acceleration, $a = a^{exp} + a^{imp}$. The explicit acceleration, a^{exp} , includes all forcing terms which depend only on the previous time step and the current position, while the implicit acceleration, a^{imp} , includes forcing terms which depend on the velocity at the current time step (in particular the drag and Coriolis forces).

Using a time step of Δt , and subscripts to denote the time step (so that $t_{n+1} = t_n + \Delta t$), the modified velocity Verlet scheme can be written as:

- 1) Calculate updated position: $x_{n+1} = x_n + u_n \Delta t + \frac{1}{2} \Delta t^2 \left(a_n^{exp} + a_n^{imp} \right)$.
- 2) Calculate a_{n+1}^{exp}
- 3) Calculate a_{n+1}^{imp} and $u_{n+1} = u_n + \frac{\Delta t}{2} \left(a_n^{exp} + a_{n+1}^{exp} \right) + (\Delta t) a_{n+1}^{imp}$

This scheme reduces to the traditional velocity Verlet when a^{imp} is set to zero. Note that $a_{n+1}^{exp} = a_{n+1}^{exp}(x_{n+1}, t_n)$ is an explicit function of x_{n+1} and other quantities evaluated at time t_n , while $a_{n+1}^{imp} = a_{n+1}^{imp}(u_{n+1}, x_{n+1}, t_n)$ additionally depends on u_{n+1} , and needs to be solved implicitly. For this reason in step three, a_{n+1}^{imp} and u_{n+1} need to be solved simultaneously, as described in the next subsection.

In equation (1), the forces due to ocean drag, atmospheric drag and sea ice drag are treated implicitly. The force due to sea surface slope and wave radiation are treated explicitly. The Coriolis term is handled using Crank-Nicolson scheme so that half of the effect is implicit and half is explicit. The elastic part of the interactive forces is treated explicitly, while the interactive damping is handled semi-implicitly in that the drag force on element A by element B depends on the velocities of elements A and B evaluated at time t_{n+1} and t_n , respectively.

655 7.2 Solving for the velocity implicitly

656 Since this modified scheme contains some forcing terms which are handled implicitly,
 657 a_{n+1}^{imp} and u_{n+1} need to be calculated simultaneously. We demonstrate how this is
 658 done, using a simplified one-dimensional version of equation (1), neglecting the atmo-
 659 spheric drag, sea ice drag and Coriolis force, so that the only implicitly treated term is the
 660 ocean drag. In this demonstration, we use a superscript to denote the ocean drag force,
 661 F^o , and ocean velocity, u^o , to avoid confusion with the subscripts indicating time step.
 662 We also define an explicit force, F^{exp} , which accounts for all forces not proportional the
 663 element velocity. With these simplifications, the implicit and explicit accelerations are

$$664 \quad a^{exp} = \frac{1}{M}(\vec{F}^{exp}) \quad (21)$$

$$a^{imp} = \frac{1}{M}(F^o) \quad (22)$$

665 The ocean drag force at time t_{n+1} is modeled (mostly) implicitly as

$$F_{n+1}^o = \tilde{c}^o |u_n^o - u_n| (u_n^o - u_{n+1}), \quad (23)$$

666 where \tilde{c}^o is the effective drag coefficient, accounting for the dimensions of the ice element
 667 (see equation 12).

668 Step 3 of the modified velocity Verlet scheme can be rewritten by introducing an
 669 intermediate velocity u^* , which only depends on the velocity and acceleration at time t_n ,

$$u_n^* = u_n + \frac{1}{2}(\Delta t)a_n^{exp}. \quad (24)$$

670 Using this, the updated velocity (Step 3) can be written

$$u_{n+1} = u_n^* + \frac{\Delta t}{2}a_{n+1}^{exp} + (\Delta t)a_{n+1}^{imp}. \quad (25)$$

671 Including the forcing terms into this equations gives

$$u_{n+1} = u_n^* + \frac{\Delta t}{2M}(F_{n+1}^{exp}) + \frac{\Delta t}{M} \left(c_w |u_n^o - u_n| (u_n^o - u_{n+1}) \right) \quad (26)$$

672 Solving for $u(t_{n+1})$ in terms of quantities which only depend on the previous time step
 673 gives

$$u_{n+1} = \frac{u_n^* + \frac{\Delta t}{2M}(F_{n+1}^{exp}) + \frac{\Delta t}{M} \left(c_w |u_n^o - u_n| (u_n^o) \right)}{\left(1 + \frac{\Delta t}{M} c_w |u_n^o - u_n| \right)} \quad (27)$$

674 Once the u_{n+1} has been found, it can be used to calculate the explicit and implicit acceler-
 675 ations, which are required for the next time step.

676 Finally, we note that the the drag term (equation 23) is not entirely implicit, since
 677 the element velocity inside the absolute value is evaluated at time t_n , rather than at time
 678 t_{n+1} . This is done so that we can solve for the updated velocity analytically. One conse-
 679 quence of this is that it can give rise to a small oscillation in the element velocity. This
 680 oscillation is addressed by using a predictive corrective scheme: after solving for a first
 681 guess of the velocity at time t_{n+1} , this estimate of the velocity is used to update the esti-
 682 mate of the drag force (i.e.: inside the absolute value signs). This updated drag, can now
 683 be used to repeat the process described above to find an improved estimate of the velocity.
 684 We found that two iterations were sufficient to remove the unwanted oscillation.

685 The procedure described in this section is easily extended to include more forcing
 686 terms and two dimensions (where it involves inverting a 2×2 matrix).

687 **8 Appendix C**

688 **Connecting bonds across processor boundaries**

689 Since the LBIM is parallelized across multiple processors, it often happens that two
 690 elements on different processes are bonded together. Keeping track of numerical bonds
 691 across processor boundaries requires a lot of book keeping. In this section we describe the
 692 how LBIM handles bonds across processor boundaries.

693 The basics of the bond bookkeeping work as follows: consider an element A and
 694 an element B that are bonded together. Each element has a copy of the bond (a piece of
 695 memory which describes the bond between the two elements), which is stored with the
 696 element. Let A-B be the bond stored by element A, and B-A be the bond stored by ele-
 697 ment B. Bond A-B contains a pointer which points to element B and bond B-A contains a
 698 pointer which points to element A.

699 Consider a situation where element A and B are originally on Processor 1, and then
 700 element B moves to Processor 2. When this occurs, the memory assigned to element B
 701 on processor 1 is removed, and is allocated on Processor 2. This means that the pointer
 702 to element B in bond A-B (stored in element A on Processor 1) is no longer assigned.
 703 Similarly, the pointer to element A in bond B-A (stored in element B on Processor 2) is
 704 no longer assigned. Before the next time step, a halo update occurs, so that the there is
 705 a copy of element A in the halo of Processor 2 and a copy of element B in the halo of
 706 Processor 1. After the halo update, the bonds A-B and B-A have to be reconnected on
 707 both Processor 1 and 2. To aid in reconnecting the bonds, a copy of the grid cell number
 708 of element B is stored in the bond A-B and a copy of the grid cell number of element A
 709 is stored in the bond B-A. We refer to this as the ‘most recent address’. Before a bond
 710 is moved from one processor to another, the ‘most recent address’ is updated, so that the
 711 bond can be reconnected later. To reconnect bond A-B on Processor 1 (for example), we
 712 find the most recent address of element B, and search through the list of elements in the
 713 grid cell corresponding to the most recent address of element B until element B is found.
 714 The pointer to element B in bond A-B is reassigned, and the bond is said to be connected.

715 The reconnected bond A-B (stored in element A) is said to be working properly
 716 when the following four test pass:

- 717 1. The pointer to element B is assigned on bond A-B.
 718 2. The corresponding bond B-A exists on element B.
 719 3. A pointer to element A exists in this bond B-A.
 720 4. The element A which is being pointed to is the same element A where you started.

721 A useful tool disconnecting and reconnecting bonds is that each element is assigned a
 722 unique number so that elements are easily identified.

723 **Acknowledgments**

724 = enter acknowledgments here =

725 **References**

- 726 Asay-Davis, X. S., S. L. Cornford, B. K. Galton-Fenzi, R. M. Gladstone, G. H. Gud-
 727 mundsson, D. M. Holland, P. R. Holland, and D. F. Martin (2016), Experimental de-
 728 sign for three interrelated marine ice sheet and ocean model intercomparison projects:
 729 MISMIP v. 3 (MISMIP+), ISOMIP v. 2 (ISOMIP+) and MISOMIP v. 1 (MISOMIP1).
 730 *Geoscientific Model Development* 9, no. 7: 2471.
- 731 Arrigo, K. R., G. L. van Dijken, D. G. Ainley, M. A. Fahnestock, and T. Markus (2002).
 732 Ecological impact of a large Antarctic iceberg. *Geophys. Res. Lett.*, 29(7).
- 733 Alley, R. B., H. J. Horgan, I. Joughin, K. M. Cuffey, T. K. Dupont, B. R. Parizek, S.
 734 Anandakrishnan, and J. Bassis (2008), A simple law for ice-shelf calving. *Science* 322,
 735 no. 5906, 1344-1344.
- 736 Bassis, J. N., and S. Jacobs (2013), Diverse calving patterns linked to glacier geometry.
 737 *Nature Geoscience*, 6(10), 833-836.
- 738 Benn, D. I., C. R. Warren, and R. H. Mottram (2007). Calving processes and the dynam-
 739 ics of calving glaciers. *Earth-Science Reviews*, 82(3), 143-179.
- 740 Bigg, G. R., Wadley, M. R., Stevens, D. P., and Johnson, J. A. (1997), Modeling the dy-
 741 namics and thermodynamics of icebergs. *Cold Regions Science and Technology*, 26(2),
 742 113-135.
- 743 Borstad, C. P., A. Khazendar, E. Larour, M. Morlighem, E. Rignot, M. P. Schodlok, and
 744 H. Seroussi (2012), A damage mechanics assessment of the Larsen B ice shelf prior to
 745 collapse: Toward a physically-based calving law, *Geophys. Res. Lett.*, 39, L18502
- 746 Biddle, L. C., J. Kaiser, K. J. Heywood, A. F. Thompson and A. Jenkins (2015), Ocean
 747 glider observations of iceberg-enhanced biological productivity in the northwestern
 748 Weddell Sea, *Geophys. Res. Lett.*, 42, 459-465.
- 749 De Rydt, J., and G. H. Gudmundsson (2016), Coupled ice shelf ocean modeling and com-
 750 plex grounding line retreat from a seabed ridge. *J. of Geophys. Res.: Earth Surface*,
 751 121(5), 865-880.
- 752 Dunne, J.P., J.G. John,, A.J. Adcroft, S.M. Griffies, R.W. Hallberg, E. Shevliakova, R.J.
 753 Stouffer, W. Cooke, K.A. Dunne, M.J Harrison, and J.P. Krasting (2012), GFDL's
 754 ESM2 global coupled climate-carbon Earth System Models. Part I: Physical formula-
 755 tion and baseline simulation characteristics. *J. of Climate*, 25(19), 6646-6665.
- 756 Depoorter, M. A., J. L. Bamber, J. A. Griggs, J. T. M. Lenaerts, Stefan RM Ligtenberg,
 757 M. R. van den Broek, and G. Moholdt (2013), Calving fluxes and basal melt rates of
 758 Antarctic ice shelves. *Nature*, 502(7469), 89-92.
- 759 Determan J., Gerdes R. (1994), Melting and freezing beneath ice shelves: implications
 760 from a three-dimensional ocean-circulation model. *Ann. Glaciol.*, 20, 413-419.
- 761 Dowdeswell, J. A., and J. L. Bamber (2007), Keel depths of modern Antarctic icebergs
 762 and implications for sea-floor scouring in the geological record. *Marine Geology*,
 763 243(1), 120-131.
- 764 Duprat, L. P., G. R. Bigg, and D. J. Wilton (2016), Enhanced Southern Ocean marine pro-
 765 ductivity due to fertilization by giant icebergs. *Nature Geoscience*.
- 766 Eckert, E. R. G. (1950). Introduction to the Transfer of Heat and Mass. McGraw-Hill.
- 767 Fogwill, C.J., E. van Sebille, E.A. Cougnon, C.S. Turney, S.R. Rintoul, B.K. Galton-Fenzi,
 768 G.F. Clark, E.M. Marzinelli, E.B. Rainsley, and L. Carter (2016), Brief communication:
 769 Impacts of a developing polynya off Commonwealth Bay, East Antarctica, triggered by
 770 grounding of iceberg B09B. *The Cryosphere*, 10(6), p.2603.
- 771 Gladstone, R. M., G. R. Bigg, and K. W. Nicholls. (2001), Iceberg trajectory model-
 772 ing and meltwater injection in the Southern Ocean (1978-2012). *J. of Geophys. Res.:*
 773 *Oceans*, 106(C9), 19903-19915.
- 774 Goldberg, D. N., C. M. Little, O. V. Sergienko, A. Gnanadesikan, R. Hallberg, and M.
 775 Oppenheimer (2012), Investigation of land ice-ocean interaction with a fully coupled
 776 ice-ocean model: 1. Model description and behavior. *J. of Geophys. Res.: Earth Surface*,
 777 117(F2).

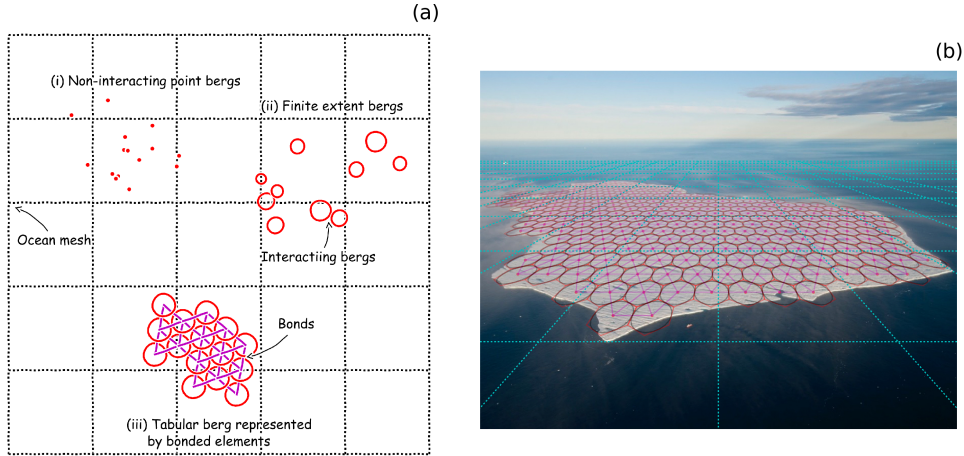
- 778 Gladish, C. V., D. M. Holland, P. R. Holland, and S. F. Price (2012), Ice-shelf basal chan-
 779 nels in a coupled ice/ocean model. *J. of Glaciol.*, 58(212), 1227-1244.
- 780 Grosfeld K., R. Gerdes, J. Determan (1997), Thermohaline circulation and interaction
 781 between ice shelf cavities and the adjacent open ocean. *J. Phys. Oceanogr.*, **102**, C7,
 782 15959-15610.
- 783 Grosfeld, K., and H. SandhŁger, (2004). The evolution of a coupled ice shelfDocean sys-
 784 tem under different climate states. *Global and Planetary Change*, 42(1), 107-132.
- 785 Hallberg, R., A. Adcroft, J. P. Dunne, J. P., Krasting, R. J., and Stouffer (2013), Sensitiv-
 786 ity of twenty-first-century global-mean steric sea level rise to ocean model formulation.
 787 *J. of Climate*, 26(9), 2947-2956.
- 788 Holland D. M., Jenkins A. (2001), Adaptation of an isopycnic coordinate ocean model for
 789 the study of circulation beneath ice shelves. *Mon. Wea. Rev.*, 129, 1905-1927.
- 790 Holland P. R. and D. L. Feltham (2006), The effects of rotation and ice shelf topography
 791 on frazil-laden Ice Shelf Water plumes. *J. Phys. Oceanogr.*, 36, 2312-2327.
- 792 Holland, D. M., and A. Jenkins (1999), Modeling thermodynamic ice-ocean interactions at
 793 the base of an ice shelf. *J. of Phys. Oceanogr.* 29.8, 1787-1800.
- 794 Hellmer H.H., Olbers D. J. (1989), A two-dimensional model for the thermohaline circula-
 795 tion under an ice shelf. *Antarctic Science*, 1, 325- 336.
- 796 Henderson J., J. S. P. Loe (2016), The Prospects andChallenges for Arctic Oil Develop-
 797 ment. *Oil, Gas and Energy Law Journal (OGEL)*, 14 (2)
- 798 Hopkins, M. A. (1996). On the mesoscale interaction of lead ice and floes. *J. of Geophys.*
 799 *Res.: Oceans*, 101(C8), 18315-18326.
- 800 Hopkins, M. A. (2004). A discrete element Lagrangian sea ice model. *Engineering Com-
 801 putations*, 21(2/3/4), 409-421.
- 802 Gaskill, H. S., and J. Rochester (1984). A new technique for iceberg drift prediction. *Cold*
 803 *Reg. Sci. Technol.*, 8(3), 223-234.
- 804 Jacobs, S. S., H. H. Helmer, C. S. M. Doake, A. Jenkins, R. M. Frolich (1992), Melting
 805 of ice shelves and the mass balance of Antarctica. *J. of Glaciol.*, 38(130), 375-387.
- 806 Jakobsen, T. (2001). Advanced character physics. In *Game Developers Conference*, Vol. 3.
- 807 Jenkins, A., P. Dutrieux, S. S. Jacobs, S. D. McPhail, J. R. Perrett, A. T. Webb, and D.
 808 White (2010), Observations beneath Pine Island Glacier in West Antarctica and implica-
 809 tions for its retreat. *it Nature Geo.*, 3(7), 468-472.
- 810 Jacobs, S. S., A. Jenkins, C. F. Giulivi, and P. Dutrieux (2011). Stronger ocean circulation
 811 and increased melting under Pine Island Glacier ice shelf. *Nature Geo.*, 4(8), 519-523.
- 812 Jongma, J. I., E. Driesschaert, T. Fichefet, H. Goosse, and H. Renssen (2009), The ef-
 813 fect of dynamic-thermodynamic icebergs on the Southern Ocean climate in a three-
 814 dimensional model, *Ocean Modell.*, 26, 104D113.
- 815 Kubat I., M. Sayed, S. Savage, T. Carrieres (2005), An operational model of iceberg drift
 816 *Int. J. Off. Polar Eng.*, 15 (2), 125D131
- 817 Lewis E.L. and R.G. Perkin (1986), Ice pumps and their rates. *J. of Geophys. Res.*, 91,
 818 11756-11762.
- 819 Losch, M. (2008). Modeling ice shelf cavities in a z coordinate ocean general circulation
 820 model. *J. of Geophys. Res.: Oceans*, 113(C8).
- 821 Li, B., H. Li, Y. Liu, A. Wang and S. Ji (2014), A modified discrete element model for
 822 sea ice dynamics. *Acta Oceanologica Sinica*, 33(1), 56-63.
- 823 Liu, M. B. and G. R. Liu (2010), Smoothed particle hydrodynamics (SPH): an overview
 824 and recent developments. *Archives of computational methods in engineering*, 17(1), 25-
 825 76.
- 826 Lichéy, C., and H. H. Hellmer (2001). Modeling giant-iceberg drift under the influence of
 827 sea ice in the Weddell Sea, Antarctica. *J. of Glaciol.*, 47(158), 452-460.
- 828 Levermann, A., T. Albrecht, R. Winkelmann, M. A. Martin, M. Haseloff, and I. Joughin.
 829 (2012), Kinematic first-order calving law implies potential for abrupt ice-shelf retreat.
 830 *The Cryosphere*, 6(2), 273-286.

- 831 Mountain, D. G. (1980). On predicting iceberg drift. *Cold Reg. Sci. Technol.*, 1(3-4), 273-
832 282.
- 833 Martin, T., and Adcroft, A. (2010), Parameterizing the fresh-water flux from land ice to
834 ocean with interactive icebergs in a coupled climate model. *Ocean Modelling*, 34(3),
835 111-124.
- 836 Marsh, R., V. O. Ivchenko, N. Skliris, S. Alderson, G. R. Bigg, G. Madec, A. T. Blaker
837 Y. Aksenov, B. Sinha, A.C. Coward, and J.L. Sommer (2015), NEMODICB (v1. 0):
838 interactive icebergs in the NEMO ocean model globally configured at eddy-permitting
839 resolution. *Geoscientific Model Development* 8, no. 5 (2015): 1547-1562.
- 840 MacAyeal D.R. (1984), Thermohaline Circulation Below the Ross Ice Shelf: A Conse-
841 quence of Tidally Induced Vertical Mixing and Basal Melting. *J. Geophys. Res.*, 89,
842 597-606
- 843 Merino, N., Le Sommer, J., Durand, G., Jourdain, N. C., Madec, G., Mathiot, P., and
844 Tournadre, J. (2016), Antarctic icebergs melt over the Southern Ocean: climatology and
845 impact on sea ice. *Ocean Modelling*, 104, 99-110.
- 846 Nicholls K.W. (1996), Temperature variability beneath Ronne Ice Shelf, Antarctica, from
847 thermistor cables. *J. Phys. Oceanogr.*, 11, 1199-1210.
- 848 Nicholls KW, Østerhus S, Makinson K (2009), Ice-Ocean processes over the continental
849 shelf of the southern Weddell Sea, Antarctica: a review. *Rev. Geophys.* 47(3).
- 850 Omelyan, I. P., M. I. Mryglod, and R. Folk (2002), Optimized Verlet-like algorithms for
851 molecular dynamics simulations. *Physical Review E*, 65(5), 056706.
- 852 Rabatel, M., S. LabbÓ and J. Weiss (2015). Dynamics of an assembly of rigid ice floes. *J.*
853 *of Geophys. Res.: Oceans*, 120(9), 5887-5909.
- 854 Rignot, E., S. Jacobs, J. Mouginot, and B. Scheuchl (2013), Ice-shelf melting around
855 Antarctica. *Science*, 341, no. 6143 (2013): 266-270.
- 856 Robinson, N. J., M. J. M. Williams, P. J. Barrett, and A. R. Pyne (2010), Observations of
857 flow and ice-ocean interaction beneath the McMurdo Ice Shelf, Antarctica, *J. Geophys.*
858 *Res.*, 115, C03025
- 859 Pizzolato, L., S. E. Howell, C. Derksen, J. Dawson, L. Copland (2014), Changing sea ice
860 conditions and marine transportation activity in Canadian Arctic waters between 1990
861 and 2012, *Climatic Change* 123 (2), 161173.
- 862 Pan, W., A. M. Tartakovsky, and J. J. Monaghan (2013). Smoothed particle hydrodynam-
863 ics non-Newtonian model for ice-sheet and ice-shelf dynamics. *J. of Comp. Phys.*, 242,
864 828-842.
- 865 Pralong, A., and M. Funk (2005), Dynamic damage model of crevasse opening and appli-
866 cation to glacier calving, *J. Geophys. Res.*, 110, B01309.
- 867 Sergienko, O. V. (2013). Basal channels on ice shelves. *J. of Geophys. Res.: Earth Surface*,
868 118(3), 1342-1355.
- 869 Silva, T. A. M., Bigg, G. R., and Nicholls, K. W. (2006), Contribution of giant icebergs to
870 the Southern Ocean freshwater flux. *J. of Geophys. Res.: Oceans*, 111(C3).
- 871 Smith, K., B. Robison, J. Helly, R. Kaufmann, H. Ruhl, H., T. Shaw, and M. Vernet
872 (2007), Free-drifting icebergs: Hotspots of chemical and biological enrichment in the
873 Weddell Sea, *Science*, 317, 478-482.
- 874 Shepherd, A., and D. Wingham (2007). Recent sea-level contributions of the Antarctic and
875 Greenland ice sheets. *Science*, 315(5818), 1529-1532.
- 876 Stern, A. A., D. M. Holland, P. R. Holland, A. Jenkins and J. Sommeria (2014), The ef-
877 fect of geometry on ice shelf ocean cavity ventilation: a laboratory experiment. *Experi-
878 ments in Fluids*, 55(5), 1-19.
- 879 Stern, A.A., Johnson, E., Holland, D.M., Wagner, T.J., Wadhams, P., Bates, R., Abraham-
880 sen, E.P., Nicholls, K.W., Crawford, A., Gagnon, J. and Tremblay, J.E. (2015), Wind-
881 driven upwelling around grounded tabular icebergs. *J. of Geophys. Res.: Oceans*, 120(8),
882 5820-5835.
- 883 Stern, A. A., A. Adcroft, and O. Sergienko (2016), The effects of Antarctic iceberg calv-
884 ing size distribution in a global climate model. *J. of Geophys. Res.: Oceans*, 121(8),

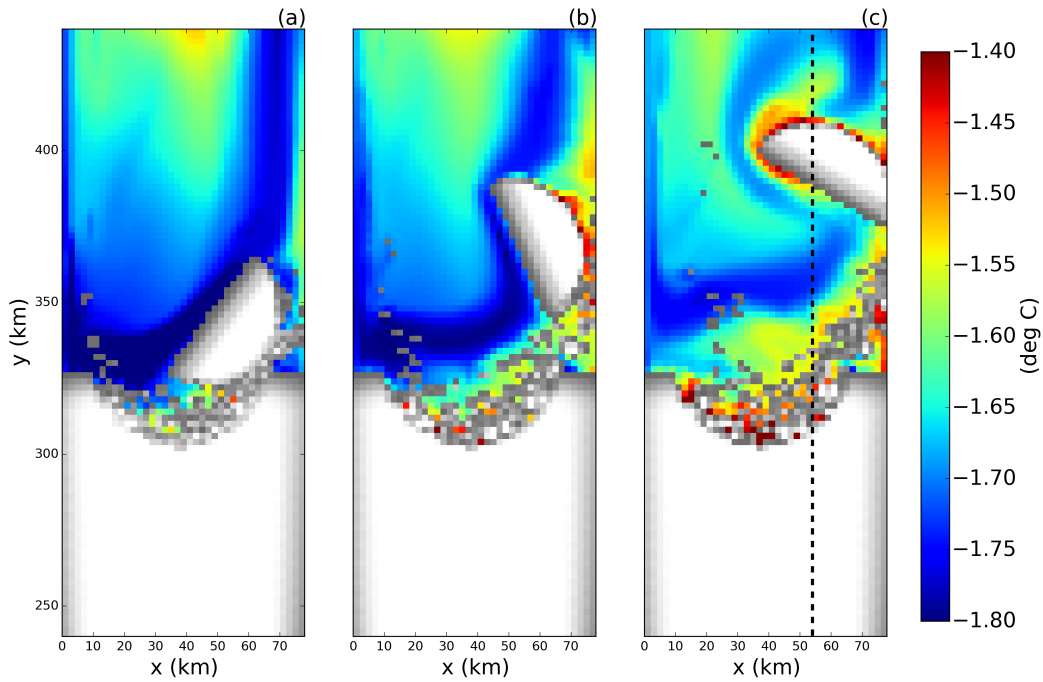
- 885 5773-5788.
- 886 Swope, W. C., H. C. Andersen, P. H. Berens, and K. R. Wilson (1982), A computer sim-
887 ulation method for the calculation of equilibrium constants for the formation of physi-
888 cal clusters of molecules: Application to small water clusters. *The Journal of Chemical*
889 *Physics* 76, no. 1, 637-649.
- 890 Tournadre, J., N. Bouhier, F. Girard-Ardhuin, and F. RÖmy (2016), Antarctic icebergs dis-
891 tributions 1992-2014. *J. Geophys Res: Oceans*.
- 892 Turnbull I.D., N. Fournier, M. Stolwijk, T. Fosnaes, D. McGonigal (2015), Operational
893 iceberg drift forecasting in Northwest Greenland, *Cold Reg. Sci. Technol.* 110, 1-18
- 894 Unger, J. D., 2014. Regulating the Arctic Gold Rush: Recommended Regulatory Reforms
895 to Protect Alaska's Arctic Environment from Offshore Oil Drilling Pollution . *Alaska L.*
896 *Rev*, 31
- 897 Vernet, M., et al. (2012), Islands of ice: Influence of free-drifting Antarctic icebergs on
898 pelagic marine ecosystems, *Oceanography*, 25(3), 38Ð39
- 899 Wagner, T. J., Wadhams, P., Bates, R., Elosegui, P., Stern, A., Vella, D., E. P. Abraham-
900 sen, A. Crawford, and Nicholls, K. W. (2014), The ÒfootlooseÓ mechanism: Iceberg
901 decay from hydrostatic stresses. *Geophys. Res. Lett.*, 41(15), 5522-5529.
- 902 Weeks, W. F., and W. J. Campbell (1973). Icebergs as a fresh-water source: an appraisal.
903 *J. of Glaciol.*, 12(65), 207-233.
- 904 White, L., A. Adcroft, and R. Hallberg (2009), High-order regridding-remapping schemes
905 for continuous isopycnal and generalized coordinates in ocean models. *J. of Comp.*
906 *Phys.*, 228(23), 8665-8692.

| Parameter | Symbol | Value | Unit |
|---|--------------|--------------------|--------------|
| Domain Length | L_x | 80 | km |
| Domain Width | L_y | 480 | km |
| Horizontal Resolution | Δx | 2 | km |
| Number of vertical layers | N_l | 72 | non-dim |
| Horizontal Viscosity | ν_H | 6.0 | $m^2 s^{-1}$ |
| Diapycnal Viscosity | ν_V | 10^{-3} | $m^2 s^{-1}$ |
| Horizontal Diffusivity | ϵ_H | 1.0 | $m^2 s^{-1}$ |
| Diapycnal Diffusivity | ϵ_V | 5×10^{-5} | $m^2 s^{-1}$ |
| Initial Surface Temperature | T_t | -1.9 | $^{\circ}C$ |
| Initial Bottom Temperature | T_b | 1.0 | $^{\circ}C$ |
| Initial Surface Salinity | S_t | 33.8 | psu |
| Initial Bottom Salinity | S_b | 34.7 | psu |
| Maximum Ocean depth | H_{ocean} | 720 | m |
| Relaxation Time of Sponge Layer | T_{sponge} | 0.1 | days |
| Length of Sponge Layer | L_{sponge} | 10 | km |
| LBIM Time Step | dt | 10 | s |
| Elastic interactive force spring constant | κ_e | 10^{-5} | $kg s^{-2}$ |

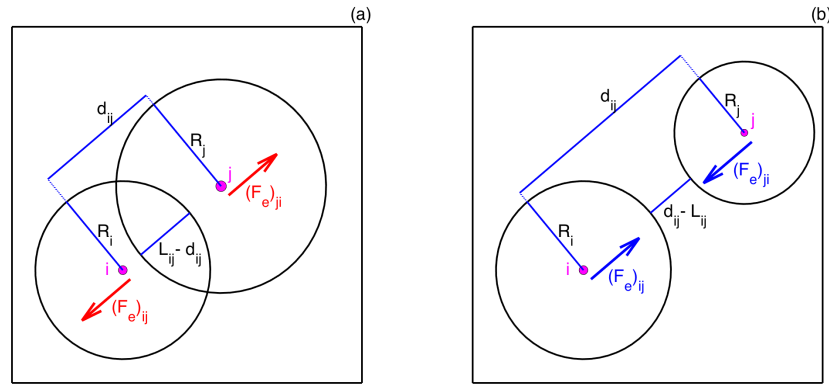
907 **Table 1.** Parameters used in the model. The ocean model parameters are as described in Asay-Davis et al
 908 [2016]



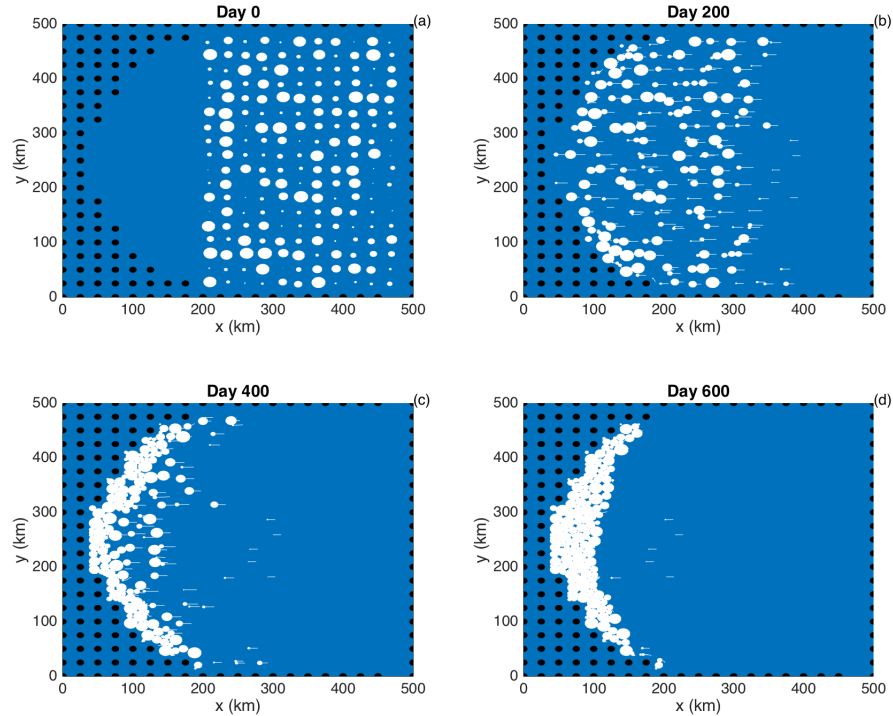
909 **Figure 1.** Schematic showing how tabular icebergs are constructed using Lagrangian elements. (a) Hierar-
 910 chy of ice elements' physical structure: (i) Previous iceberg models represent icebergs using non-interacting
 911 point-particle elements. (ii) In the LBIM ice elements are given finite extent so that they are able to inter-
 912 act with the ocean across multiple grid cells, and can interact with other elements. (iii) These finite extent
 913 elements can be joined together by numerical bonds (magenta lines) to form larger structures such as tabular
 914 icebergs. (b) Areal photograph of a tabular iceberg with elements superimposed over it to illustrate how
 915 the Lagrangian elements can be used to model tabular icebergs. In this schematic the ice elements (purple
 916 dots) are initialized in a staggered lattice covering the surface area of the iceberg. For purposes of mass ag-
 917 gregation, the ice elements are assumed to have hexagonal shape (red hexagons). For purposes of element
 918 interactions, the ice elements are assumed to be circular (black circles). Elements are initially bonded to adja-
 919 cent elements using numerical bonds (magenta lines). These numerical bonds form equilateral triangles which
 920 give the shape rigidity. Ocean grid lines have been included (dashed cyan lines). The background photo is an
 921 areal photograph of iceberg PIIB (Area= 42 km²) taken in Baffin Bay in 2012. A red ship can be identified on
 922 the bottom of the photo for scale.



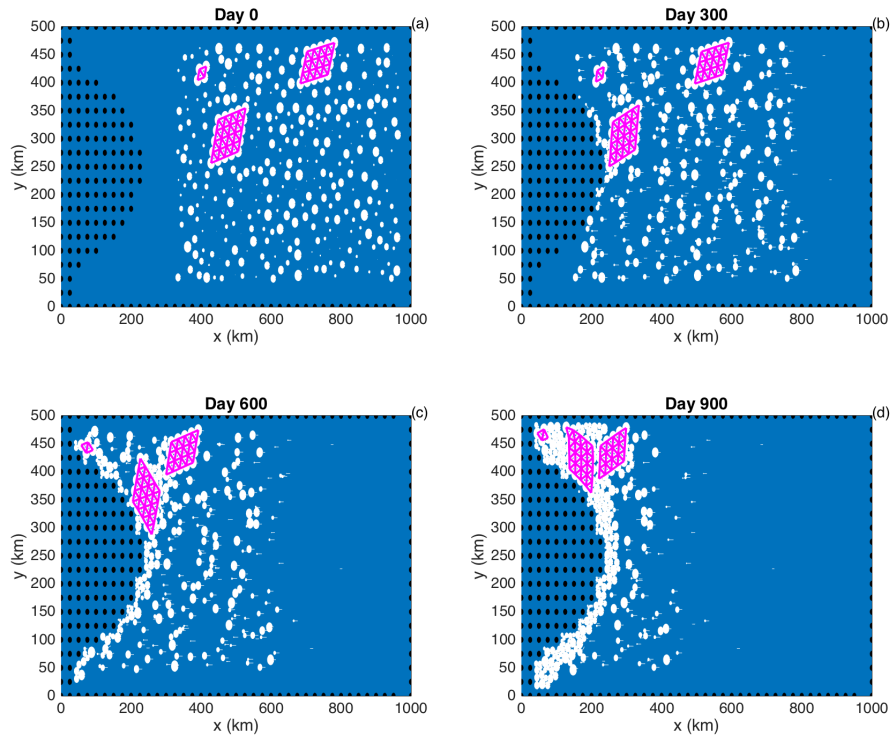
923 **Figure 2.** Snapshots of the sea surface temperature in the LBIM tabular iceberg calving simulation. Snap-
924 shots are taken (a) 7, (b) 15, and (c) 30 days after calving. Grid cells with ice mass $> 10^4$ kg are plotted in
925 white, with grey shading indicating thinner ice. The dashed line in panel (c) shows the location of the vertical
926 transects shown in Figures 8 and 11.



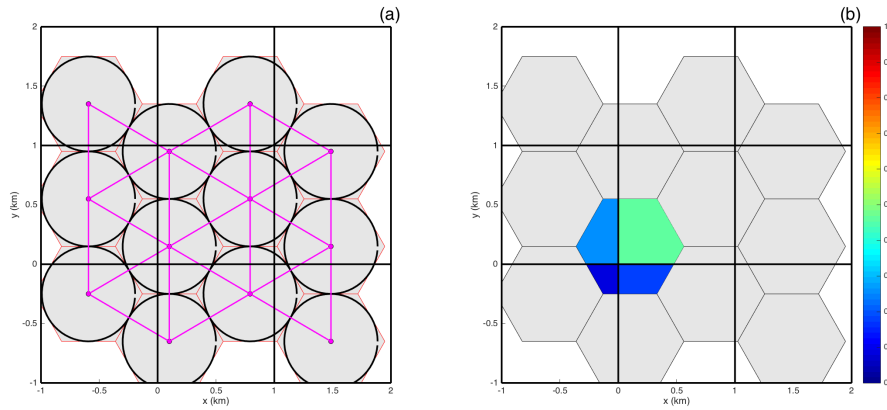
927 **Figure 3.** Diagram showing the (a) repulsive and (b) attractive elastic interactive forces between two ele-
 928 ments, i and j . R_i and R_j are the interactive radii of element i and j , respectively. d_{ij} is the distance between
 929 the centers of elements. $L_{i,j} = R_i + R_j$ is the critical-interaction-length scale. $(F_e)_{ij}$ and $(F_e)_{ji}$ are the elastic
 930 forces applied to elements i and j , respectively (equation 7). A frictional damping force is also applied, which
 931 opposes the relative velocity of the elements (not shown). The attractive forces are only applied when the two
 932 elements are bonded together (i.e.: $B_{ij} = 1$).



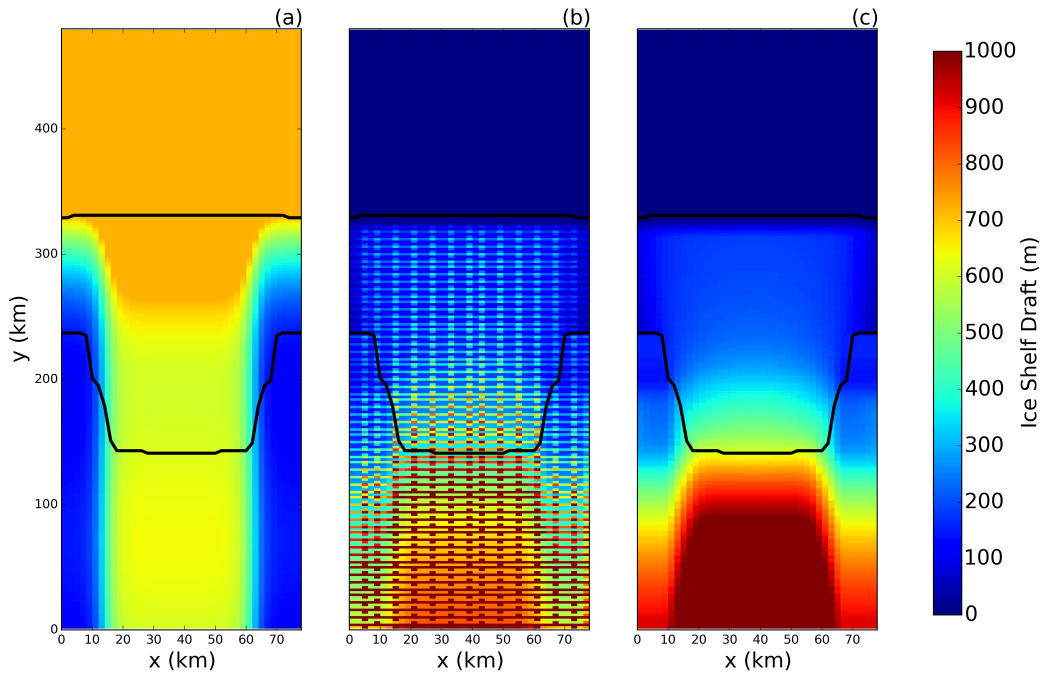
933 **Figure 4.** Results of an ice-only LBIM simulation with no bonds between ice elements. Ice elements are
 934 initialized throughout the domain, as shown in panel (a). The elements are forced by an imposed westward
 935 ocean current of $u=0.1\text{m/s}$ (no ocean model is used). Forces due to sea surface slope, atmospheric drag, Cori-
 936 olis and sea ice drag are set to zero. The figure shows snapshots of ice element positions at time (a) $t=0$, (b)
 937 200, (c) 400, (d) 600 days. The size of the dots shows the surface area (and interaction radius) of each ice
 938 element. The white tails behind the elements show the elements' positions over the preceding two days. Land
 939 points are shown by black circles.



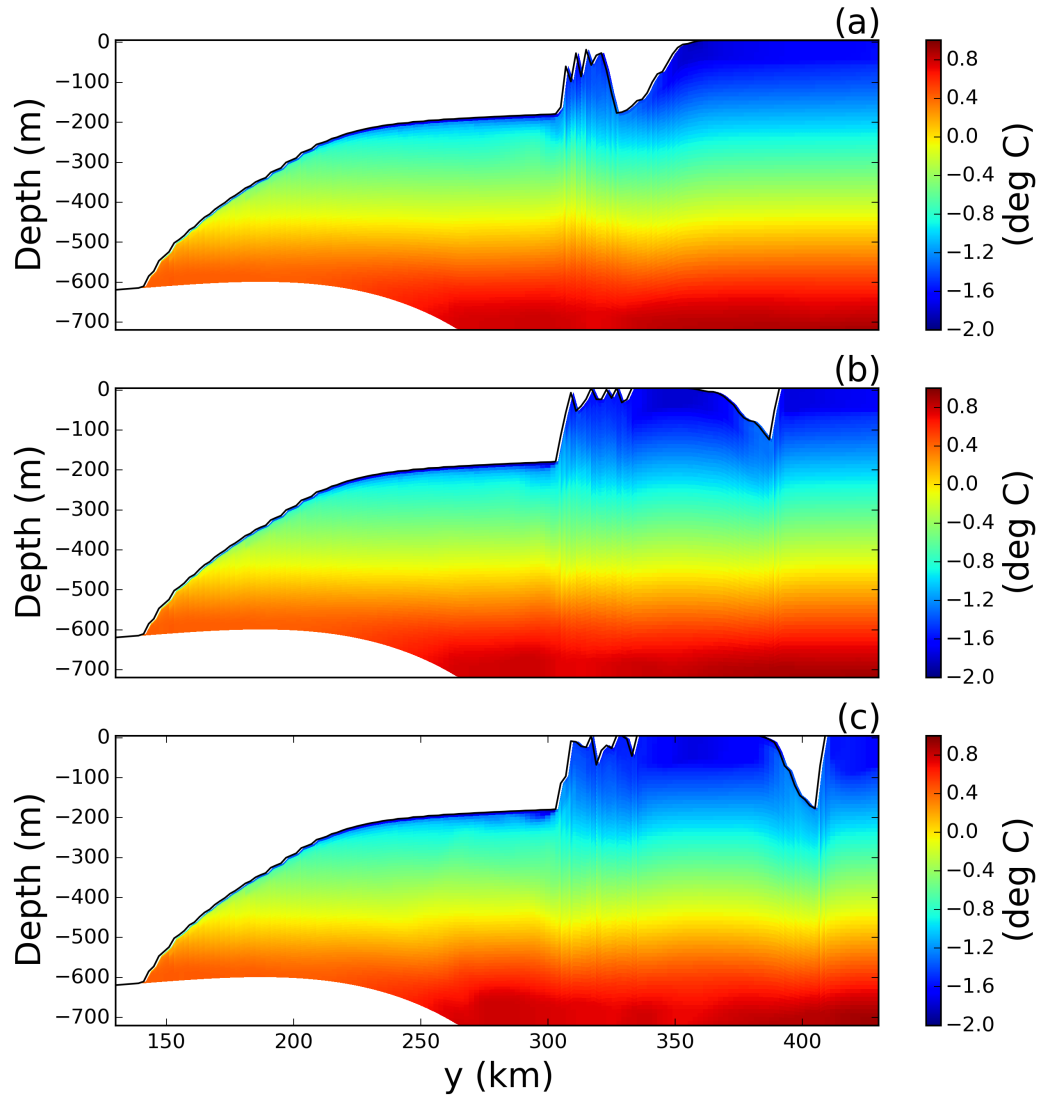
940 **Figure 5.** Results of an ice-only LBIM simulation using bonds between elements. Ice elements are ini-
 941 tialized throughout the domain, as shown in panel (a). Three tabular icebergs are included, with 25, 16 and
 942 4 elements respectively. The elements are forced by an imposed westward ocean current of $u=0.1\text{m/s}$ (no
 943 ocean model is used). Forces due to sea surface slope, atmospheric drag, Coriolis and sea ice drag are set to
 944 zero. The figure shows snapshots of ice element positions at time (a) $t=0$, (b) 300, (c) 600, (d) 900 days. The
 945 size of the dots shows the surface area (and interaction radius) of each ice element. The white tails behind the
 946 elements show the elements' positions over the preceding two days. Bonds between ice elements are plotted
 947 in magenta. Land points are shown by black circles.



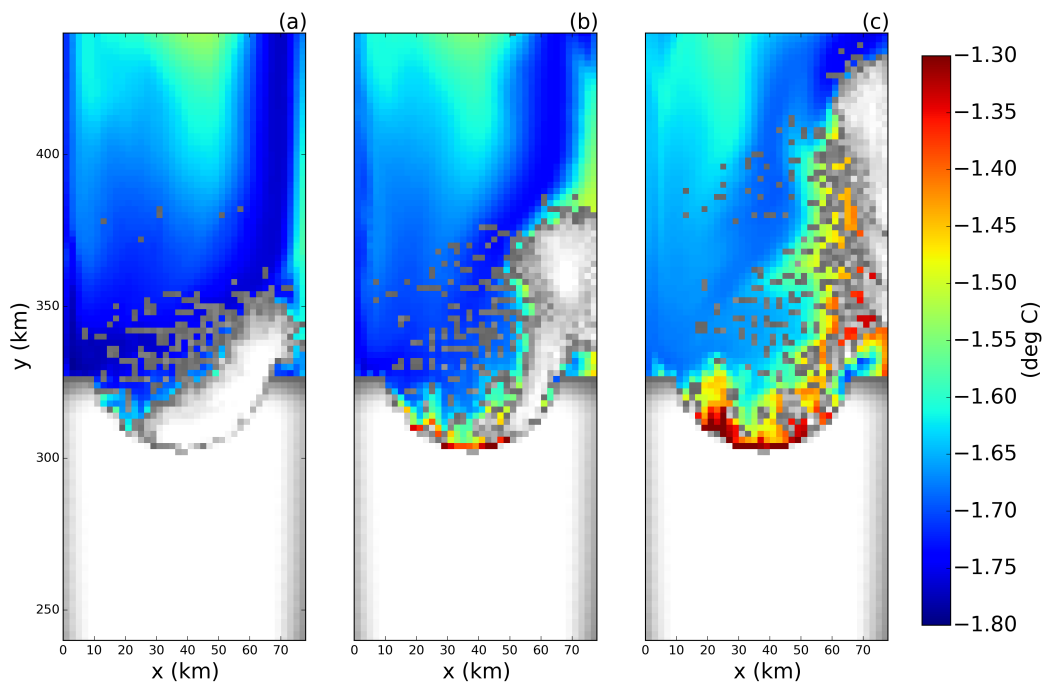
948 **Figure 6.** (a) Ice element packing and geometry: ice elements (purple dots) are initialized in a stag-
949 gered lattice. For purposes of mass aggregation, the ice elements are assumed to have hexagonal shape (red
950 hexagons). For purposes of element interactions, the ice elements are assumed to be circular (black circles).
951 Elements are initially bonded to adjacent elements using numerical bonds (magenta lines). (b) Intersec-
952 tion of an hexagonal element and the ocean grid. The colors indicate the fraction of the hexagon that lies in each
953 grid cell. These fractions are used as weights to spread LBIM properties to the ocean grid (see text for more
954 details).



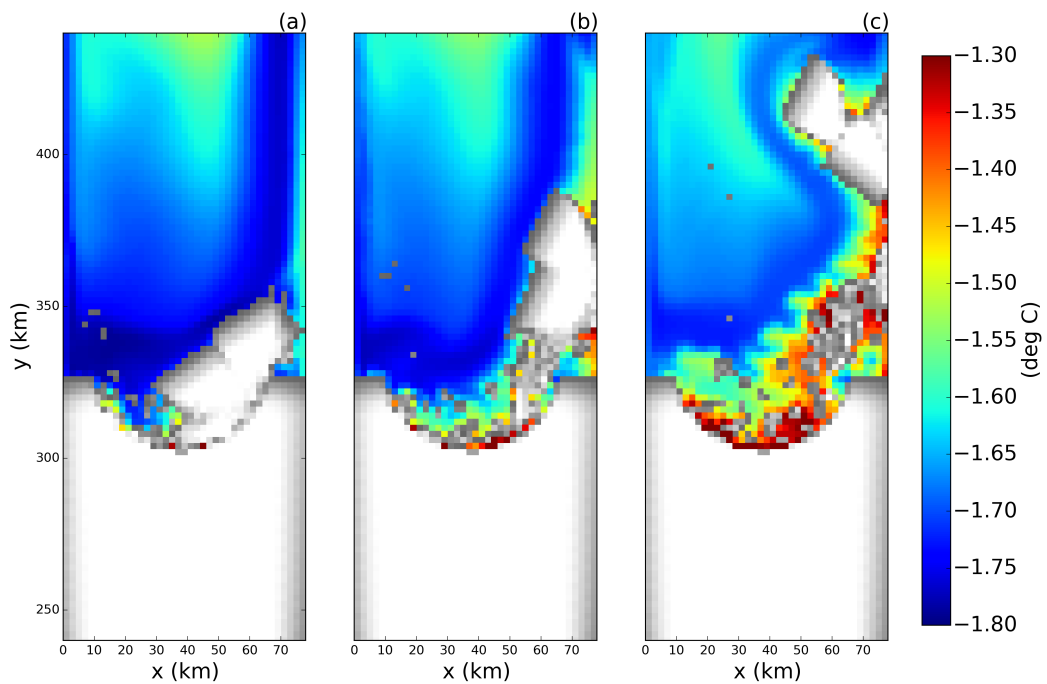
955 **Figure 7.** (a) Ocean bottom topography and (c) ice-shelf draft used to initialized the tabular iceberg calv-
956 ing simulation. The ice draft is calculated from the total mass in an ocean grid cell after the mass-spreading
957 interpolation has been applied (as explained in Section 2.3). Panel (b) shows the initial ice draft that would be
958 calculated if the mass-spreading interpolation were not used (i.e.: elements treated as point masses).



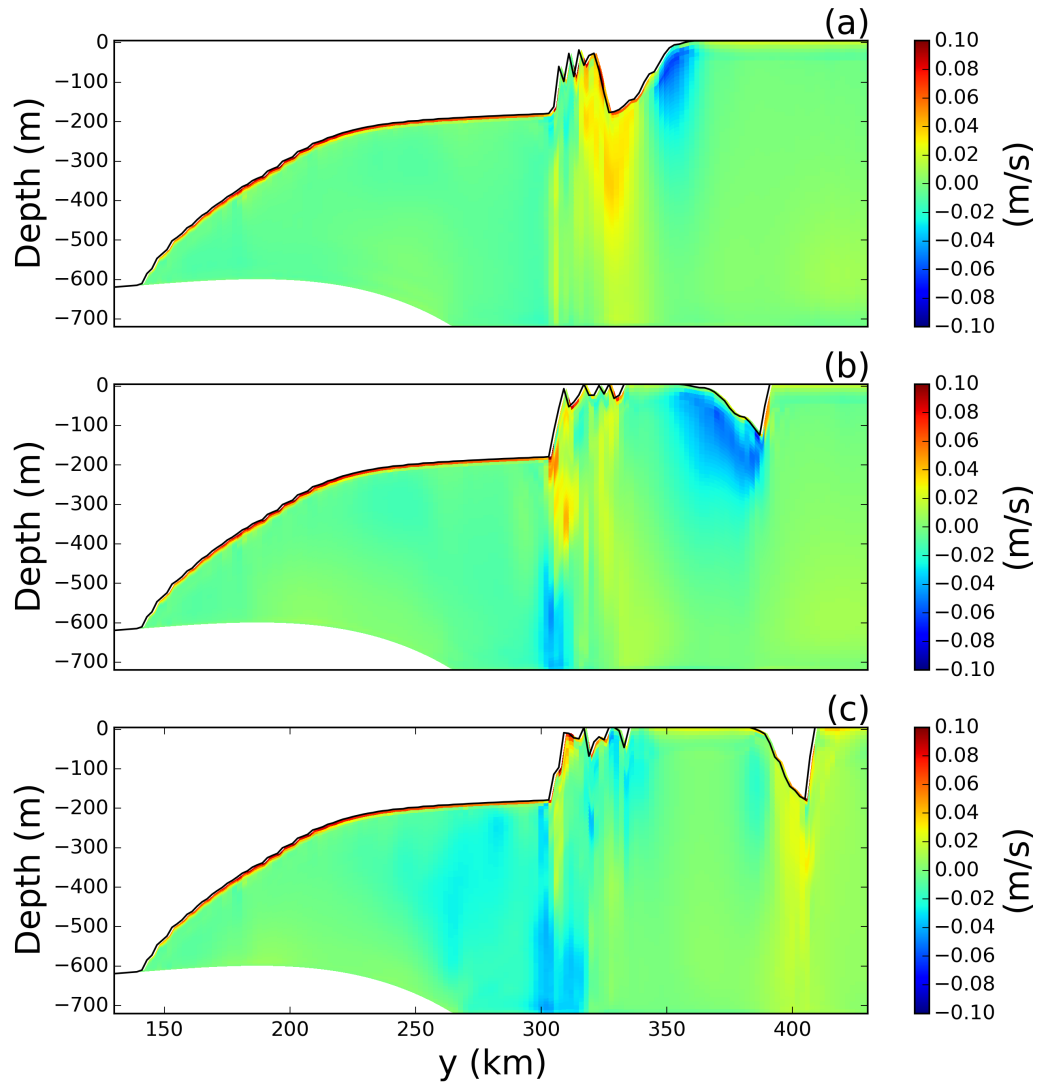
959 **Figure 8.** Snapshots of vertical sections of ocean temperature at $x=54$ km in the tabular-iceberg-calving
 960 control experiment. Snapshots are taken (a) 7, (b) 15, and (c) 30 days after calving. The position of the
 961 vertical transects is shown by the dashed lines in Figure 2c.



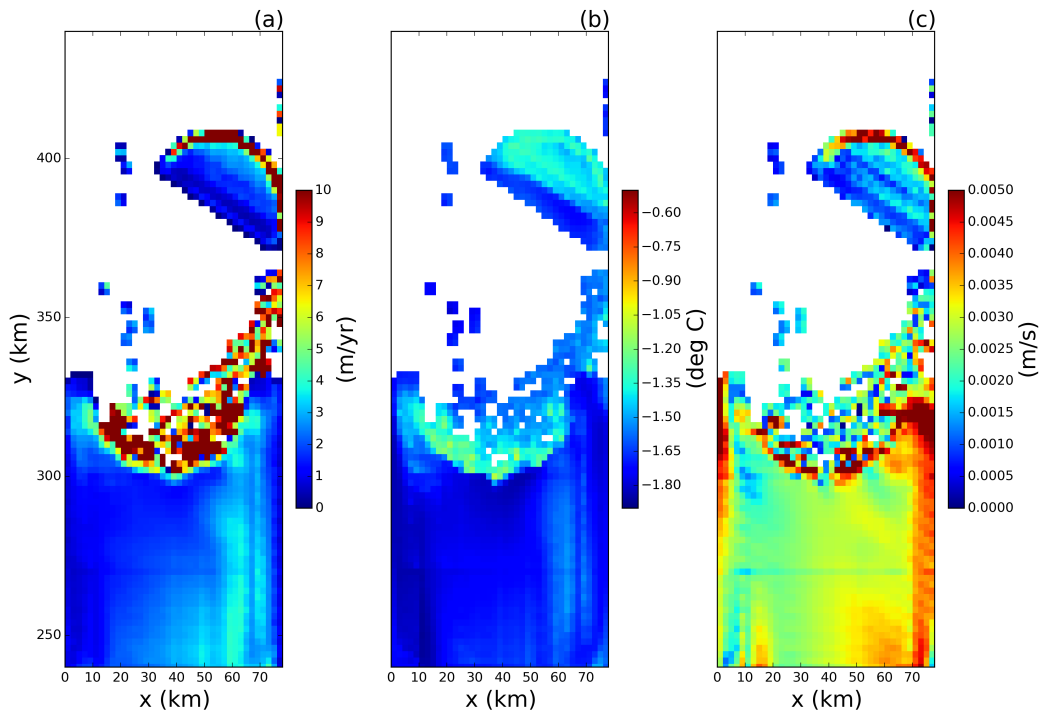
962 **Figure 9.** No bonds simulation: Snapshots of the sea surface temperature for a simulation where all bonds
963 have been broken. Snapshots are taken (a) 7, (b) 15, and (c) 30 days after calving. Grid cells with ice mass >
964 10^4 kg are plotted in white, with grey shading indicating thinner ice.



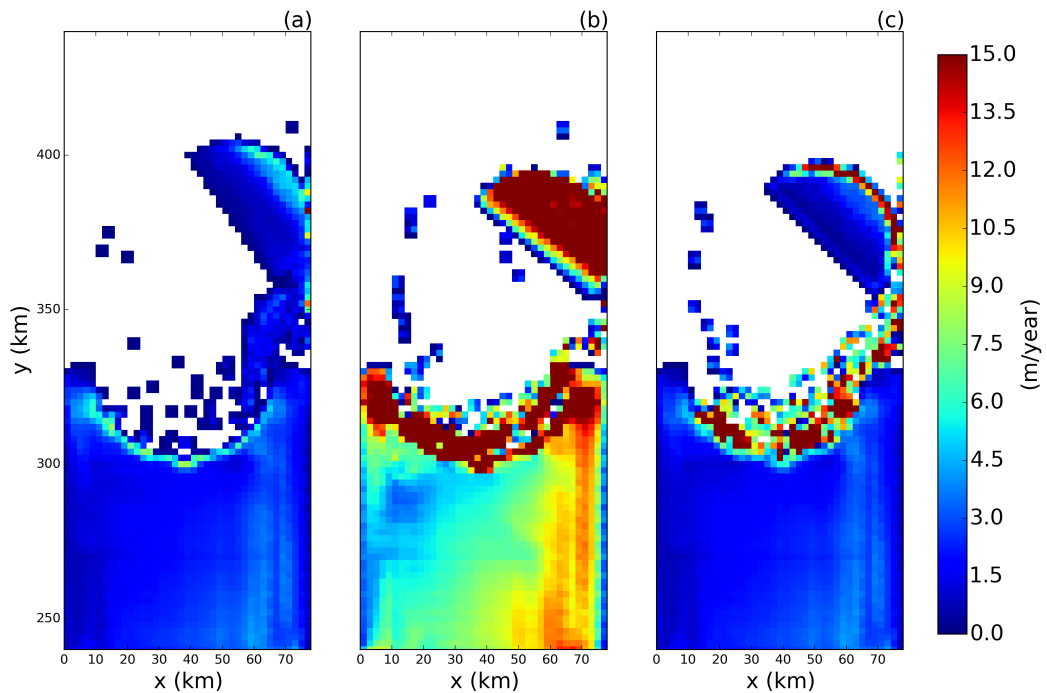
965 **Figure 10.** Iceberg splitting simulation: Snapshots of the sea surface temperature for the iceberg splitting
966 simulation. Snapshots are taken (a) 7, (b) 15, and (c) 30 days after calving. Grid cells with ice mass $> 10^4$ kg
967 are plotted in white, with grey shading indicating thinner ice.



968 **Figure 11.** Snapshots of vertical sections of meridional velocity at $x=54$ km in the tabular-iceberg-calving
 969 control experiment. Snapshots are taken (a) 7, (b) 15, and (c) 30 days after calving. The position of the
 970 transects is shown by the dashed line in Figure 2c.



971 **Figure 12.** Results of the tabular-iceberg-calving experiment 30 days after the iceberg calves. The three
972 panels show snapshots of the (a) melt rate, (b) top-of-ocean temperature and (c) u^* at the base of the ice shelf.
973 Fields are only shown in regions where the ice area fraction is ≥ 0.8 .



974 **Figure 13.** Results of the tabular-iceberg-calving experiment using three different melt-rate parametra-
975 tion. Panels show snapshots of the melt rate 30 days after calving for simulations using the (a) three-equation
976 melt-rate parametrization, (b) icebergs-drift melt-rate parametrization, (c) mixed-melt-rate parametrization (as
977 described in Section 2.5.)

978

9 **Supplementary Material**

979

The experiment configuration used to initialize the calving-tabular-iceberg simulation
980 (in this study) is the same as that of the Ocean0 setup in the MISOMIP, with the follow-
981 ing three changes made:

982

- 983 1. The ‘calving criteria’ used in the MISOMIP study (which states that all points in
the ice shelf with thickness less than 100m are set to zero thickness) has not been
used.
- 985 2. The ice shelf has been thickened on the flanks of the domain, so that the latitude of
the grounding line increases away from the center of the ice shelf.
- 986 3. The ice shelf is configured to be symmetric about its meridional center line ($x =$
988 $\frac{L_x}{2}$). This was achieved by using the average of the left and right flanks of the ice-
989 shelf thickness.

990

These three changes were made in order to make the circulation beneath the ice shelf eas-
991 ier to interpret.